Article

Numerical Analysis of the Breakdown Process of CF$_3$I at Low Pressure

Yifan Wu [1], Zhijiang Wang [1,*], Hao Wu [2] and Wei Jiang [1,3]

1   State Key Laboratory of Advanced Electromagnetic Technology, International Joint Research Laboratory of Magnetic Confinement Fusion and Plasma Physics, School of Electrical and Electronic Engineering, Huazhong University of Science and Technology, Wuhan 430074, China; m202172014@hust.edu.cn (Y.W.); weijiang@hust.edu.cn (W.J.)
2   School of Electronics and Information Engineering, Hubei University of Science and Technology, Xianning 437100, China; haowulearning@gmail.com
3   School of Physics, Huazhong University of Science and Technology, Wuhan 430074, China
*   Correspondence: wangzj@hust.edu.cn

Featured Application: The research discussed in this paper sheds light on the breakdown behavior of CF$_3$I under low atmospheric pressure conditions. This understanding is beneficial for expanding its use in applications like plasma etching and thin film deposition. By delving into the specifics of CF$_3$I breakdown, this study helps pave the way for its improved and wider application in various technological fields.

Abstract: The breakdown of CF$_3$I gas at low pressure is of significant importance for applications in fields such as aerospace and microelectronics. However, the DC low-pressure breakdown characteristics of CF$_3$I remain underexplored. In this work, we utilize a one-dimensional implicit particle-in-cell/Monte Carlo collision (PIC/MCC) algorithm to investigate the complete DC breakdown process of low-pressure CF$_3$I. Our model accounts for ion–molecule collisions, recombination reactions, and external circuit influences. The breakdown process is delineated into three stages: before breakdown, breakdown, and after breakdown. In the before-breakdown stage, both the density and energy of particles are low. In the breakdown stage, the rapid increase in electron density and energy accelerates ionization reactions, leading to successful breakdown. The circuit behavior transitions from capacitive to resistive, sharing voltage with the external resistance. In the after-breakdown stage, continued positive ion growth leads to the formation of a thin anode sheath and a negative plasma potential. Energy production, including heating power and secondary electron emission (SEE) power, balances with energy loss through collision and boundary absorption. Specifically, 62% of the total heating power comes from positive ions, 1.5% from negative ions, and approximately 85% of electron energy is lost via boundary absorption. Finally, we compare the Paschen curves of CF$_3$I with those of SF$_6$, providing insights that are beneficial for the application of CF$_3$I as an SF$_6$ alternative.

Keywords: particle simulation; gas breakdown; CF$_3$I; Paschen curve

1. Introduction

Many studies have pointed out that sulfur hexafluoride (SF$_6$) is a greenhouse gas with serious environmental impacts [1,2]. Consequently, SF$_6$ has been listed as one of the six regulated greenhouse gases [3]. Many scientists are looking for alternative gases to reduce the use of SF$_6$ [4–6].

Trifluoroiodomethane (CF$_3$I) has been proposed as an environmentally friendly alternative to SF$_6$ due to its low global warming potential (GWP) of less than 5, a short atmospheric lifetime of 0.005 years, and zero ozone depletion potential [7]. Furthermore, CF$_3$I has shown advantageous safety characteristics, non-toxicity, flame retardant properties, as well as oil solubility and good material compatibility [8]. Moreover, CF$_3$I has

been explored as a fire extinguishing agent, a component in mixed refrigerants, a fluorine-containing intermediate, and a semiconductor etching gas [9].

There are a large number of studies on the breakdown characteristics of CF_3I. These studies can be broadly categorized into studies under high-pressure conditions and studies under low-pressure conditions, depending on the operating conditions.

Studies on the breakdown characteristics of CF_3I under high pressure are often related to application scenarios such as electrically insulated equipment. Zhao et al. investigated different ratios of CF_3I-N_2 gas mixtures as well as CF_3I-CO_2 gas mixtures by means of simulation. The results show that CF_3I-N_2 and CF_3I-CO_2 mixtures have better insulating properties than SF_6 at certain mixing ratios [10]. Xiaoxing Zhang et al. experimentally investigated the breakdown voltage of CF_3I-N_2 gas mixtures under different electric fields. The experimental results show that CF_3I-N_2 gas mixtures have excellent insulating properties. This indicates that CF_3I has the potential to replace SF_6 as an insulating gas for electrical equipment [11]. Yunkun Deng et al. also experimentally investigated the effects of various factors on the insulating properties of CF_3I-N_2 gas mixtures. The results show that the insulating properties of CF_3I-N_2 gas mixtures are strengthened as the proportion of CF_3I increases. In a non-uniform electric field, the CF_3I-N_2 gas mixture breakdown voltage is enhanced with an increase in the discharge gap or an increase in pressure, which is characterized by a linear increase. However, in an extremely homogeneous electric field, the breakdown voltage of the CF_3I-N_2 gas mixture does not continue to increase linearly when the gap is increased to some extent, showing a saturation characteristic [12]. You-ping Tu et al. explored the emission and decomposition of discharge by-products of CF_3I-N_2 mixed gas under high pressure through experiments. They analyzed the influence of by-products on electrically insulated switchgear [13]. Y Cressault et al. studied the insulating properties of gas mixtures such as CF_3I-N_2, CF_3I-CO_2, and CF_3I-air in high-voltage circuit breakers. The results of the study show that the gas mixtures have excellent insulation properties, are more friendly to the atmosphere, and have nontoxic by-products. However, CF_3I also has problems surrounding high boiling points and easy liquefaction [14]. Takuto Kobayashi et al. modeled an insulated transmission line using a mixture of CF_3I and CO_2 as an insulating gas. It was noted that the CF_3I-CO_2 mixture is more sensitive to the uneven electric field. This weakens its insulating performance in an inhomogeneous electric field weaker than SF_6-CO_2 gas mixture [15]. Jia Wei et al. investigated the electrical breakdown characteristics of the CF_3I-CO_2 mixture in a supercritical state, observing a discontinuity in dielectric strength near the critical point [16].

In addition, the breakdown characteristics of CF_3I under low-pressure conditions have been a significant focus in various applications. Within the realms of pulse discharge, thin film deposition, etching, and chemical catalysis, investigating the breakdown of CF_3I under low-voltage discharge conditions has substantial practical significance [17]. For example, Jiao Zhang et al. investigated the pulse discharge characteristics of helium and CF_3I gas mixtures in a chemical oxygen iodine laser by numerical simulation with a one-dimensional fluid model. The density of iodine atoms produced by the discharge was shown to increase when the pulse width and pulse voltage amplitude increased. And there exists an optimal mixing ratio between helium and CF_3I, at which the concentration of iodine atoms can be reached to reach the maximum value after discharge [18]. In a related study, Jianqiu Hou et al. explored the application of CF_3I in the realm of high-aspect-ratio low-temperature dielectric etching. Their findings suggested a minimal risk of arc and posited that the research experience with CF_3I could be extrapolated to other gases containing halogens [19].

Therefore, it is clear that the study of CF_3I, both under high- and low-pressure conditions, has considerable research value. In general, a large number of experimentally based studies have been conducted in the field of CF_3I, providing valuable information. However, obtaining sufficient information on particle kinematics through purely experimental methods is challenging. In particular, CF_3I, as a polyatomic gas, undergoes many reactions during the discharge process, producing a large number of particles and thus changing

the distribution of the space charge and the electric field. This makes it difficult to obtain microscopic information, such as the spatial distribution of the particle density, by purely experimental means. This problem can be avoided by studying CF_3I by simulation.

In recent years, studies on electronegative gases have focused mainly on the steady state. Few studies have been conducted on the process of gas breakdown under low-pressure conditions. The breakdown process under low-pressure conditions is closely related to practical applications such as pulse discharges and semiconductor processing and is of great research value. Therefore, in order to better understand the physical process of breakdown under low-pressure conditions, further research in this area is necessary. Some researchers have already realized this problem and launched studies. For example, Wu recently used the PIC/MCC program to successfully investigate the double frequency breakdown process of Ar [20], offering a potential avenue to study the low-voltage breakdown process of other gases. Gao further used the PIC/MCC method to explore the low voltage DC breakdown process of SF_6 [21]. However, few studies have explored the breakdown characteristics of CF_3I under DC low-pressure conditions.

Since the PIC/MCC method facilitates the analysis of variations in various particle parameters throughout the breakdown process, this paper will employ this model to examine CF_3I, an alternative gas to SF_6. The objective is to thoroughly investigate the breakdown process of CF_3I under low-pressure conditions.

This article is divided into five parts, as follows: In Section 2, the physical model and numerical method are presented and the principle of the research method utilized in this paper is elucidated. In Section 3, the simulation results are presented, and the changes in parameters (including particle density, current density, particle energy, and heating power) of electrons, positive ions, and negative ions over 150 µs are analyzed in depth. In Section 4, the particle equilibria, the power equilibria, and the Paschen curves are given. Section 5 provides the conclusion of this paper.

2. Models

In this paper, the breakdown process of CF_3I is investigated by combining physical modeling with numerical methods. The physical model is utilized to describe the plasma breakdown process, while the numerical method is utilized to solve the equations of motion. The simulation results help in gaining insight into the physical process of plasma breakdown.

2.1. Physics Models

The detailed principles of the physical model can be found in [22]. This section focuses on the electron–molecule collision model, the ion–molecule collision model, the recombination model, and the external circuit model.

2.1.1. Electron–Molecule and Ion–Molecule Collision

Our models include electrons, one negative ion (I^-), and four positive ions (I^+, CF_3^+, CF_3I^+, CF_2I^+), with CF_3I as the background gas. The reactions considered include an attachment, an elastic collision, a vibration, five excitations, and four ionizations. Figure 1 presents the reaction cross-sections, focusing only on key reactions that significantly influence the discharge process.

It should be noted that in the study conducted by S. Kawaguchi et al. [23], the ionization reactions considered include seven positive ions, three more ions than our data (namely CF_2^+, CF^+, and CI^+). However, the original cross-section data are not provided in the paper, making them impossible to use. Furthermore, the generation of CF_2^+, CF^+, and CI^+ requires the breaking of multiple chemical bonds, resulting in higher reaction thresholds and smaller cross-sections. By comparing the cross-sections, it can be observed that the ionization cross-sections for generating CF_2^+, CF^+, and CI^+ are one to two orders of magnitude smaller than those for generating I^+, CF_3^+, CF_3I^+, and CF_2I^+, thus rendering them negligible. The dataset used in this study comes from the Troitsk Institute of Innovation and Fusion Research

(TRINITI) in Russia, available at https://us.lxcat.net/cache/635b483e31117/ (accessed on 14 June 2024) [24]. We consider TRINITI's simplification of ionization cross-sections acceptable.
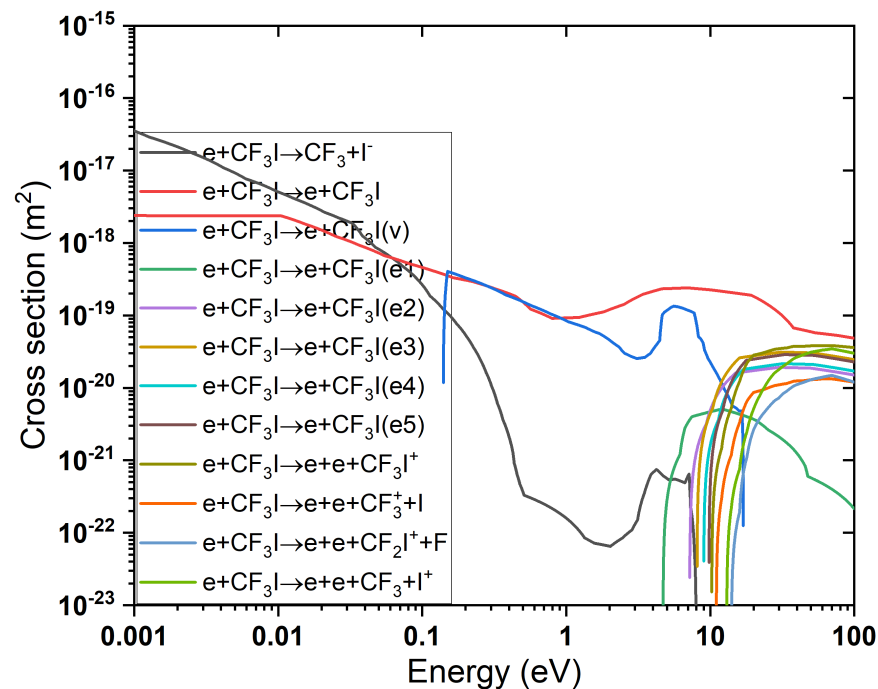

Figure 1. Collision cross-sections of e— CF_3I.

Regarding the choice of the ions I^- over F^-: The bond energy of the C-F bond in CF_3I is 5.044 eV, while the bond energy of the C-I bond is 2.496 eV. The nearly two-fold difference in bond energies indicates that the C-I bond is more susceptible to breaking during collisions, resulting in more I^- ions from electron attachment reactions. In the study by L.G. Christophorou et al., the cross-section for the formation of F^- ions is lower than that for I^- ions by about two orders [25]. Therefore, we only consider the I^- ions.

Fluorine atoms, I_2, and C_2F_6 may also be produced during the reaction, but their densities are too low to be significant and can therefore be ignored.

This paper utilizes the method proposed by Nanbu [26,27] to construct a standard MCC model. The reaction rate is determined by the Rice–Ramsperger–Kassel (RRK) theory [28]. The probability of ion collision is calculated by (1):

$$P_c = \left(\frac{\pi \alpha_p e^2}{\varepsilon_0 \mu} \right)^{1/2} \beta_\infty^2 n_g \Delta t \tag{1}$$

where α_p represents the molecular polarizability of CF_3I, which is equal to $20.0 a_0^3$ [29,30], a_0 denotes the Bohr radius, e is the electron charge, ε_0 is the vacuum dielectric constant, $\mu = m_i m_n / (m_i + m_n)$ is the reduced mass, and m_i and m_n are the ion and neutral mass, respectively. The parameter β_∞ is the cutoff value of the dimensionless shock parameter β, generally chosen as 3, and n_g is the density of CF_3I gas.

Appendix A provides the reaction formulas and threshold energies for ion–molecule collisions. Detailed calculation formulas can be found in the study by Georgieva V. et al. [22].

2.1.2. Recombination

Recombination between positive and negative ions includes $I^- - CF_3I^+$, $I^- - I^+$, $I^- - CF_2I^+$, and $I^- - CF_3^+$. In this model, a method proposed by Nanbu and Denpoh [28,31] is used to simulate the recombination between positive and negative ions. The method

divides the space into small grids and calculates the collision probabilities between positive and negative ions inside each grid using the Equation (2):

$$P_{ij} = k_0 \Delta t / \Delta V \tag{2}$$

where $k_0 = 10^{-13} \ m^3 s^{-1}$ for ion-ion recombination.

It is worth noting that CF$_3$I has a high adsorption capacity for electrons, resulting in an electron density during breakdown that often is one percent or even one-thousandth of the density of positive ions. Furthermore, the reaction coefficient for electron-positive ion recombination is more than an order of magnitude smaller than that for ion-ion recombination [21]. The combined effect of these two factors renders the impact of electron-positive ion recombination on the simulation results extremely small and therefore negligible.

2.1.3. External Circuit

When studying the gas DC breakdown process, the external resistor plays an indispensable role, both in practical experiments and simulations.

In practical experiments, the gas breakdown discharge occurrence leads to a significant increase in plasma density between the two polar plates, consequently causing a dramatic rise in conductivity. Without an external resistor in the circuit, there is a risk of damaging the experimental equipment.

During simulations, the external resistance facilitates the attainment of steady-state discharge and enables more accurate determination of electrical characteristics. Prior to gas breakdown, the system comprising the polar plate and the CF$_3$I gas inside it can be likened to a capacitor. As the gas undergoes breakdown, the system of plates and CF$_3$I exhibits resistor-like behavior from a circuit perspective. At this juncture, the external resistor serves as a voltage divider. With increasing plasma current, according to Ohm's theorem, the partial pressure on the outer resistor also rises, thereby reducing the voltage between the two pole plates, restraining the upward trend of current, and performing the dual function of voltage division and current limitation. Without the addition of an external resistor and direct application of supply voltage to the two plates for discharge simulation, the discharge may fail to reach a steady state due to the absence of a resistor to regulate the negative feedback of the voltage [20]. The simulation results can be adversely affected by either excessively large or small resistors: an excessively large resistor excessively divides voltage, resulting in insufficient voltage between the plates for gas penetration; an excessively small resistor fails to achieve the desired voltage division and current limitation effect. Additionally, it has been noted that when employing the PIC/MC model for DC breakdown simulation, the absence of external resistance in the model leads to inaccurate data such as current, thereby hindering accurate analysis of electrical characteristics [20].

An appropriate external resistance value ensures that the external resistor shares approximately 20% of the voltage when the reaction reaches a steady state. Through the calculation of the equivalent resistance of the plasma and systematic exploration of external resistance parameters, we determined that setting the external resistance to 8 kΩ is more optimal.

The circuit diagram of the equipment simulated in this paper is depicted in Figure 2. The electrodes have a circular shape. Its diameter is 0.2 m. The distance between the electrodes is 2 cm. The pressure of CF$_3$I gas between plates is maintained at 160 mTorr unless otherwise specified, a pressure low enough to induce the decomposition of CF$_3$I gas.
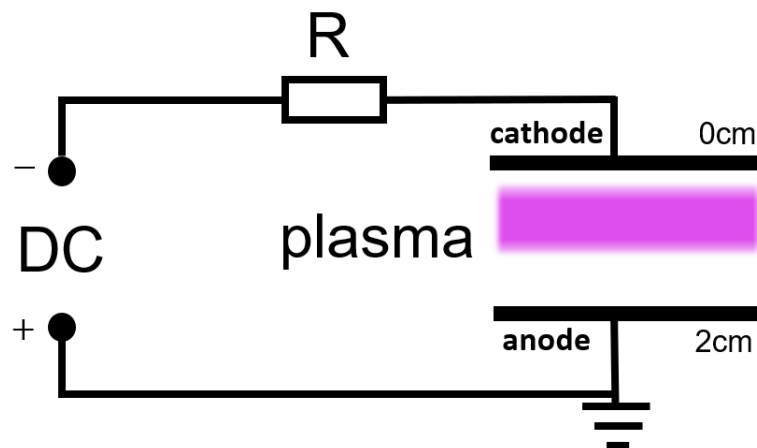
Figure 2. Diagram of external circuits.

In practical scenarios, the circuit voltage does not instantaneously reach a peak; instead, it rises rapidly from 0 to a peak of -1000 V. To simulate this phenomenon, a voltage function in the form of $1000\left(e^{-\frac{t}{1\times 10^{-10}}} - e^{-t}\right)$ was employed. Plotting the function using appropriate software revealed that the rapid transition of voltage from 0 V to -1000 V occurs within approximately 1 ns, consistent with the actual scenario.

Following the approach advocated by J.P. Verboncoeur et al. [32], the linkage between the external circuit and the plasma can be established and resolved. Subsequently, the PIC algorithm is employed to simulate the electrical parameters of each grid within the plasma over a unit of time. Solving Poisson's equation enables the determination of the potential for the plasma region situated between the parallel plates.

2.2. Numerical Methods

In recent decades, numerical methods for simulating the evolution of plasma breakdown processes have been widely explored, resulting in the development of two prominent algorithms: the explicit algorithm and the implicit algorithm. The latter has demonstrated distinct advantages over the former, providing accurate evolution parameters for the plasma breakdown process and expanding its applicability, which is unattainable for the explicit algorithm [33–36]. Numerous studies have been conducted to enhance the implicit method [20,21,37–39].

Hao Wu et al. successfully applied an improved implicit algorithm to numerically simulate the evolution of parameters in the electrical breakdown process of dual frequency (DF) capacitively coupled plasma (CCP) [20]. Similarly, Jiamao Gao et al. successfully utilized this algorithm to simulate SF_6 breakdown [21]. Consequently, this paper adopts the one-dimensional implicit "evolution" PIC/MCC algorithm.

The initial plasma density is set to 10^{10} m^{-3}. The value of the initial density does not significantly affect the breakdown process [40]. In the simulation of gas breakdown at low pressure, it is common practice to set the initial density of the plasma [20,21]. An initial density of 10^{10} m^{-3}, which is much lower than the plasma density after breakdown occurs, does not affect the nature of the breakdown. During the initialization phase, the density of positive ions is established at half of the electron density. This step ensures electrical neutrality and minimizes the effect of charge imbalance on the electric field. Particles reaching the boundary are absorbed by the electrodes, while secondary electrons are generated by ion bombardment of the electrodes, an essential factor in the growth of the electron number [20,41]. The emission energy of secondary electrons is randomly distributed within the range of 0–5 eV, and their emission direction is also randomized [42]. The ion-induced secondary electron emission coefficient is assumed to be 0.2. The secondary electron emission coefficient and the energy of secondary electrons are not the focus of

this study, but secondary electrons are essential in gas breakdown. Since the secondary electron emission coefficient for CF_3I could not be found, a value of 0.2 was adopted based on studies of SF_6 by other researchers [21,43]. The discharge gap between plates is divided into 97 grids, each initially populated with 2000 macroscopic particles. The number of grids and the spatial step of the simulation program are determined by considering equipment performance and simulation time factors to ensure accurate results. Theoretically, a smaller time step Δt results in a higher degree of decoupling between motion and collisions [21]. Given CF_3I's strong electronegativity, a longer time is required for its discharge to reach a stable state. Setting Δt too small would extend the simulation time excessively. The time step must strike a balance that is sufficient for accuracy, but not exceeding the device's calculation performance. This paper carried out tests with various time steps (1×10^{-10} s, 5×10^{-11} s, 2.5×10^{-11} s, 1×10^{-11} s, 1×10^{-12} s) and found that until Δt increases to 5×10^{-11} s, the accuracy of the calculation remains consistent. Therefore, the paper suggests that selecting $\Delta t = 5 \times 10^{-11}$ s is the most appropriate.

The diagnostic frequency is fixed at 1×10^8 Hz, corresponding to a diagnostic period of 10 ns, with each diagnostic period containing 200 time steps. This frequency setting ensures diagnostic results of a manageable size, facilitating image creation and result analysis. The duration of the full simulation spans 15,000 diagnostic cycles, totaling 150 μs.

3. Results

3.1. General Consideration

To facilitate the analysis of simulation results, the whole process is distinguished as the before-breakdown stage, the breakdown stage, and the after-breakdown stage, which is illustrated in Figure 3.

Since the breakdown process occurs within a very short time span and it takes considerably longer to reach the stabilization stage, the length of the time axis in the graph is not set in proportion to the actual time. In addition, different applied voltages and air pressures affect the breakdown time, and the time nodes in the graph are specific to the simulation parameters outlined in this section.
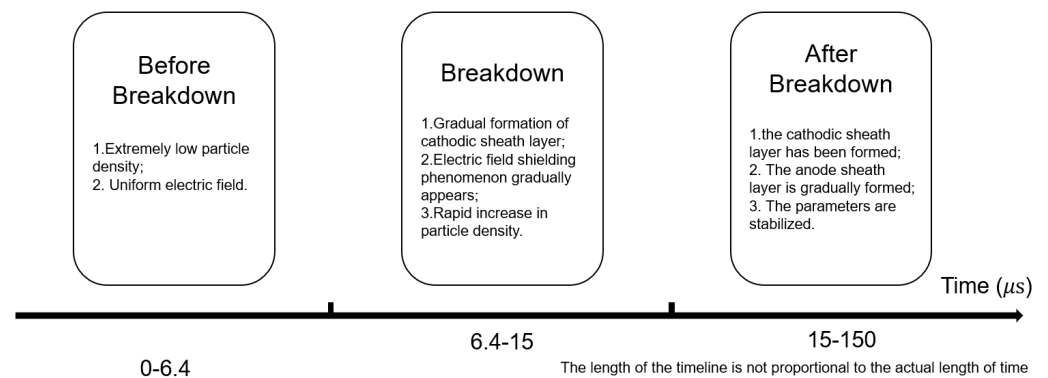

Figure 3. Flowchart of the breakdown process: divided into before-breakdown stage, breakdown stage, and after-breakdown stage.

During the before-breakdown stage, the electric field uniformly permeates the polar plate. In the breakdown stage, the reaction is very violent, which leads to the formation of the cathode sheath. The after-breakdown stage can be divided into the anode sheath formation phase and the stable phase, distinguished by the presence or absence of a stable anode sheath. During the anode sheath formation phase of the after-breakdown stage, the density and distribution of charged particles undergo gradual changes. In the stable phase of the after-breakdown stage, the anode sheath becomes clearly visible, and various parameters such as particle density, energy, current density, and heating power stabilize.

Table 1 presents the evolution of the density and energy parameters for electrons, negative ions, and positive ions. Here, $\bar{n}$ and $\bar{E}$ denote the spatial average density and energy, respectively.

Table 1. Density and Energy Evolution of Electron, Negative Ion and Positive Ion.

Stage	Before Breakdown	Breakdown	After Breakdown
t (μs)	$0 \to 6.4$	$6.4 \to 15$	$15 \to 150$
$\bar{n}_e$ (m^{-3})	$10^{10} \to 10^{8} \to 7 \times 10^{11}$	$7 \times 10^{11} \to 4.7 \times 10^{13}$	$4.7 \times 10^{13} \to 10^{12}$
$\bar{n}_{I^-}$ (m^{-3})	$10^{10} \to 3 \times 10^{11}$	$3 \times 10^{11} \to 4 \times 10^{15}$	$4 \times 10^{15} \to 10^{16}$
$\bar{n}_{I^+}$ (m^{-3})	$5 \times 10^{9} \to 3.4 \times 10^{13}$	$3.4 \times 10^{13} \to 1.1 \times 10^{15}$	$1.1 \times 10^{15} \to 10^{15}$
$\bar{n}_{CF_3^+}$ (m^{-3})	$5 \times 10^{9} \to 6.5 \times 10^{13}$	$6.5 \times 10^{13} \to 6.3 \times 10^{14}$	$6.3 \times 10^{14} \to 10^{15}$
$\bar{n}_{CF_3 I^+}$ (m^{-3})	$5 \times 10^{9} \to 9.5 \times 10^{13}$	$9.5 \times 10^{13} \to 1.4 \times 10^{15}$	$1.4 \times 10^{15} \to 10^{15}$
$\bar{n}_{CF_2 I^+}$ (m^{-3})	$5 \times 10^{9} \to 2.4 \times 10^{13}$	$2.4 \times 10^{13} \to 5.1 \times 10^{14}$	$5.1 \times 10^{14} \to 10^{15}$
$\bar{E}_e$ (eV)	37	$37 \to 79 \to 43$	$43 \to 15$
$\bar{E}_{I^-}$ (eV)	$13 \to 5.4$	$5.4 \to 1$	<1
$\bar{E}_{I^+}$ (eV)	14	$14 \to 10$	10
$\bar{E}_{CF_3^+}$ (eV)	18	$18 \to 11$	11
$\bar{E}_{CF_3 I^+}$ (eV)	13	$13 \to 10$	10
$\bar{E}_{CF_2 I^+}$ (eV)	13	$13 \to 10$	10

The density of electrons initially experiences a slight decrease in the before-breakdown stage, followed by a substantial increase in the subsequent stage. During the breakdown stage, the ionization reaction intensifies, further augmenting the electron density. In the after-breakdown stage, the fully formed cathode sheath induces an electric field shielding effect, leading to a gradual decrease in electron energy. The slow decrease in electron density during this stage is attributed to the dominance of adsorption reactions at lower electron energies.

The density of negative ions (I$^-$) steadily increases throughout the breakdown process. When no breakdown occurs, the uniform penetration of the electric field between the polar plates drives the negative ions away from the cathode, where they are energized by the force of the electric field. In the after-breakdown stage, the electric field close to the anode is weakened, causing I$^-$ to primarily distribute in the bulk region. This distribution results from the shielding of the electric field in the bulk region, leading to lower electron energies and predominantly adsorption reactions. Being heavy ions with low mobility, I$^-$ primarily resides in the bulk region and does not get accelerated by the electric field, leading to a rapid decrease in negative ion energy to less than 1 eV.

The density of positive ions experiences a significant increase in the before-breakdown stage, followed by a continued rise by one to two orders of magnitude in the breakdown stage, and eventual slowing down in the after-breakdown stage. The phenomenon of electric field shielding is absent in the before-breakdown stage, allowing the electric field to penetrate through the entire polar plate and greatly enhance positive ion energy. In the after-breakdown stage, the cathode sheath forms, and positive ions, characterized by their large mass and low mobility, gradually become confined to the cathode sheath by strong electric fields.

3.2. Electron Kinetics

Figure 4 gives the two-dimensional distribution of the four parameters of the electron's density, current density, energy, and heating rate in time and space.
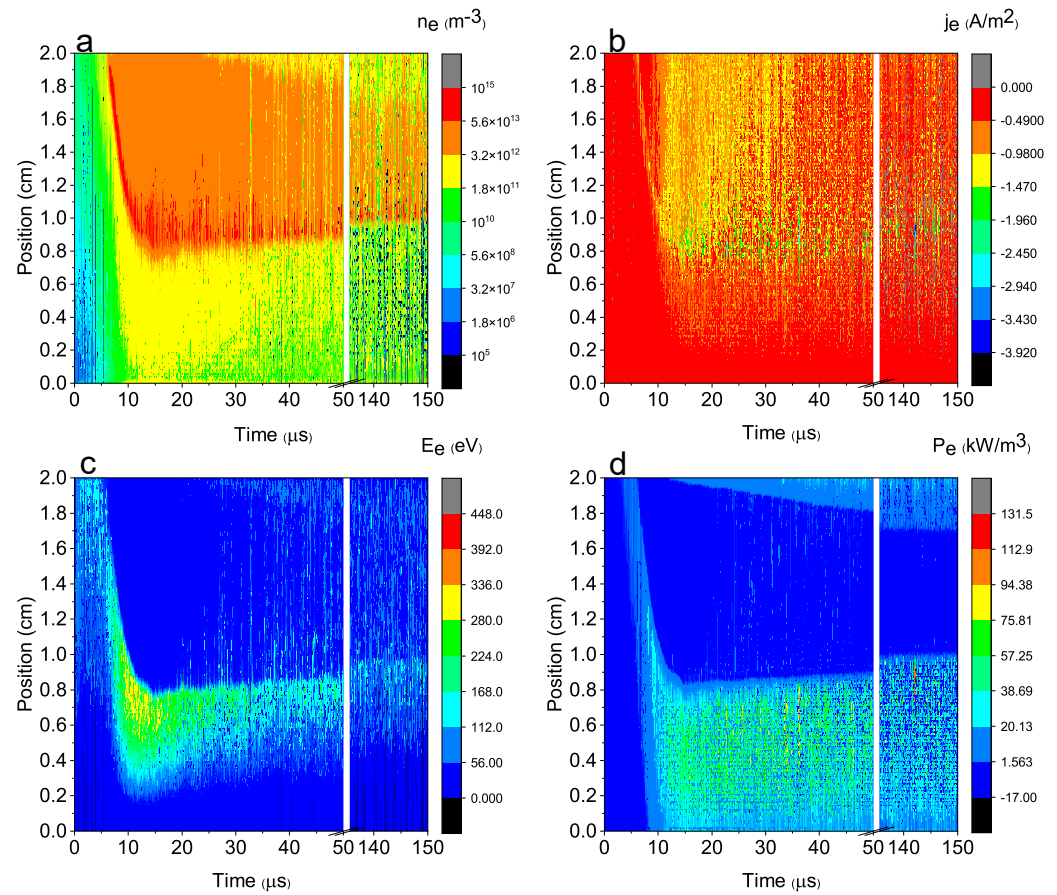
Figure 4. Spatiotemporal distribution of (**a**) electron density, (**b**) electron current density, (**c**) average electron energy and (**d**) electron heating rate.

During the time period of 0–6.4 µs, which constitutes the before-breakdown stage, the electric field permeates the entire polar plate region. A parallel electric field points from the anode to the cathode within the 0–2 cm polar plate space, generated by the negative voltage source. As electrons are attracted to the anode and accelerated in the electric field, their energy increases closer to the anode. As depicted in Figure 4c, electrons near the negative plate possess energies of approximately 10 eV, while those close to the positive plate reach energies of about 70 eV due to electric field acceleration. As shown by the collision cross-section in Figure 1, at higher electron energies, the ionization reaction predominates due to the larger cross-section, whereas the adsorption reaction rate remains small. Thus, ionization reactions become dominant in regions with higher electron energy, while the rate of adsorption reactions is low. The collision of higher energy electrons with CF_3I molecules initiates the ionization reaction, leading to the generation of more electrons and a significant increase in electron density near the anode region. However, electron energy near the cathode is only about 10 eV, insufficient to trigger enough ionization reactions to replenish electron density losses. During the before-breakdown stage, electron density at 2 cm (i.e., at the anode plate) rises to 5×10^{12} m^{-3}, while density at 0 cm (i.e., at the cathode plate) is only 10^9 m^{-3}, with an average density of 7×10^{11} m^{-3}. This indicates a tenfold increase in electron density relative to the initial density during the before-breakdown stage. Electron current density is consistently negative because electron motion is from the cathode to the anode. The absolute value of electron current density remains below 1 Am^{-2} during the before-breakdown stage, indicating very low electron current due to insufficient electron density. Additionally, as depicted in Figure 4d, the heating rate of electrons remains below 10 kWm^{-3}. These parameters indicate that reactions during the before-breakdown stage are considerably less vigorous than during the breakdown stage. Notably, the overall electron density experiences a slight decrease before rising during the

before-breakdown stage. This decrease is attributed to the small mass and high mobility of electrons, causing initial electrons near the anode to be rapidly lost under the influence of the electric field. However, as electrons from other locations migrate toward the anode after being accelerated by the electric field, ionization reactions are triggered, leading to a rapid rebound in electron density near the anode.

The breakdown stage ranges from 6.4 µs to 15 µs. During this stage, the formation of the cathode sheath begins at 6.4 µs and is complete at 15 µs. The electron density increases dramatically at this stage because of the electron avalanche. The bulk region's range begins to expand while electron density within the bulk region rises. The electron density within the bulk region reaches approximately 10^{13} m^{-3}. In the gradually forming cathode sheath, the electron density ranges between 10^{11} m^{-3} and 10^{12} m^{-3}. At this stage, the cathode sheath contains more positive than negative charges, resulting in a positive net charge, while the bulk region maintains electrical neutrality with an equal distribution of positive and negative charges. The electric field originating from the unequal charge distribution decelerates electrons, leading to lower electron energies within the bulk region. In contrast, in the cathode sheath, the electric field significantly intensifies due to the reduced distance despite the nearly identical potential difference, thus accelerating electrons to higher energies within the cathode sheath. Abnormally high energy electrons with energies exceeding 250 eV or more are observed in the cathode sheath, while in the bulk region, the electron energy remains below 20 eV. The absolute values of the electron current density within the bulk region reach 1.75 Am^{-2}, while within the cathode sheath, the values range between 0.25 Am^{-2} and 1.5 Am^{-2}, with higher densities closer to the bulk region. Notably, the electron energy within the cathode sheath experiences significant enhancement during the breakdown stage, while the electron current density does not increase proportionately. Regarding the electron heating rate, the heating rate within the bulk region remains very low, approximately 1 kWm^{-3} or less, due to the shielding of the electric field. In contrast, the heating rate within the cathode sheath is markedly high, generally exceeding 20 kWm^{-3}, attributed to the strong electric field within the sheath.

The 15–90 µs time period corresponds to the phase of formation of the anode sheath in the after-breakdown stage when a stable cathode sheath has formed. The thickness of the cathode sheath is about 0.8 cm.

After 90 µs, which corresponds to the stable phase of the after-decomposition stage, a stable anode sheath has formed, and the thickness of the anode sheath is approximately 0.3 cm. In comparison, it is found that the anode sheath is much thinner than the cathode sheath. As the stable sheath has been formed, the electric field in the bulk region is shielded, so that the electron energy in the bulk region will gradually decrease, and when the electron energy decreases to a certain low value, the adsorption reaction will dominate over the ionization reaction, and thus the electron density will gradually decrease. As shown in Figure 4a, the density of electrons in the cathode sheath is 10^{11} m^{-3} and in the bulk region it is 10^{13} m^{-3}, and the density in the anode sheath is similar to that of the cathode sheath and is also about 10^{11} m^{-3}. The general average density is 10^{12} m^{-3}, which has been significantly reduced compared to the overall average density of 10^{13} m^{-3} at 15 µs. As shown in Figure 4c, the electrons gained greater energy in the cathode sheath and the anode sheath, respectively. The electron energy of the anode sheath is about 20 eV and that of the cathode sheath is about 50 eV. The electron energy in the bulk region is very small. As shown in Figure 4d, the electron heating rate of the cathode sheath is about 20 kWm^{-3}, the anode sheath is 7 kWm^{-3}, and the heating rate of the bulk region is basically kept at a low value of less than 1 kWm^{-3}.

3.3. Positive Ion Kinetics

Positive ions encompass I$^+$, CF$_3^+$, CF$_3$I$^+$, and CF$_2$I$^+$. The spatial and temporal distributions of positive ions are shown in Figures 5–8.
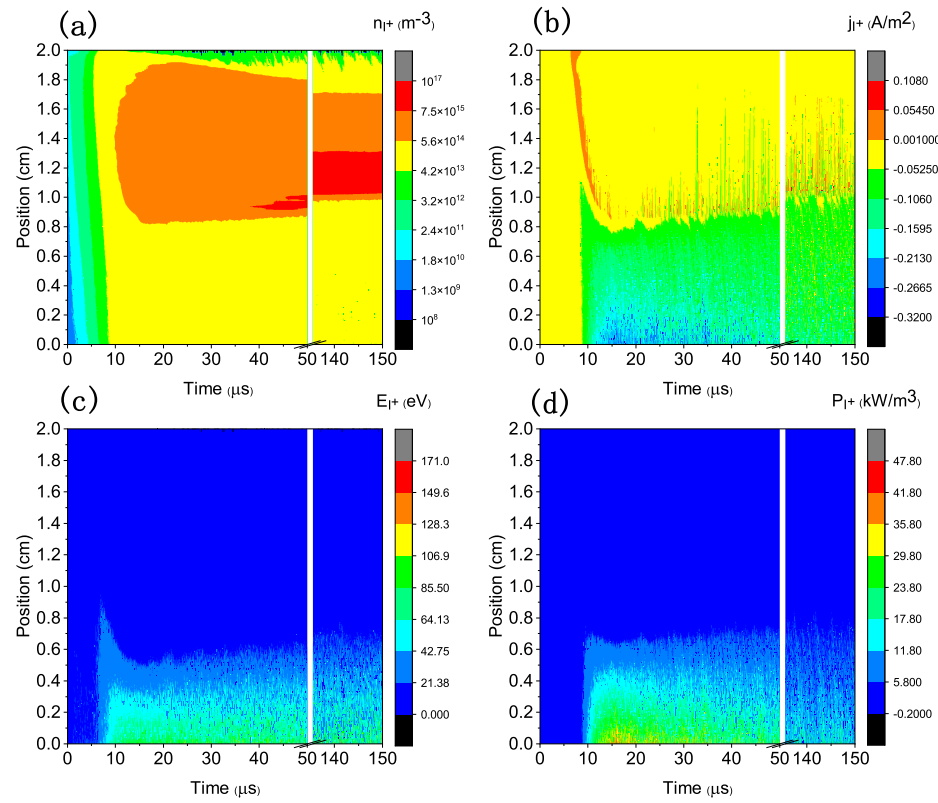
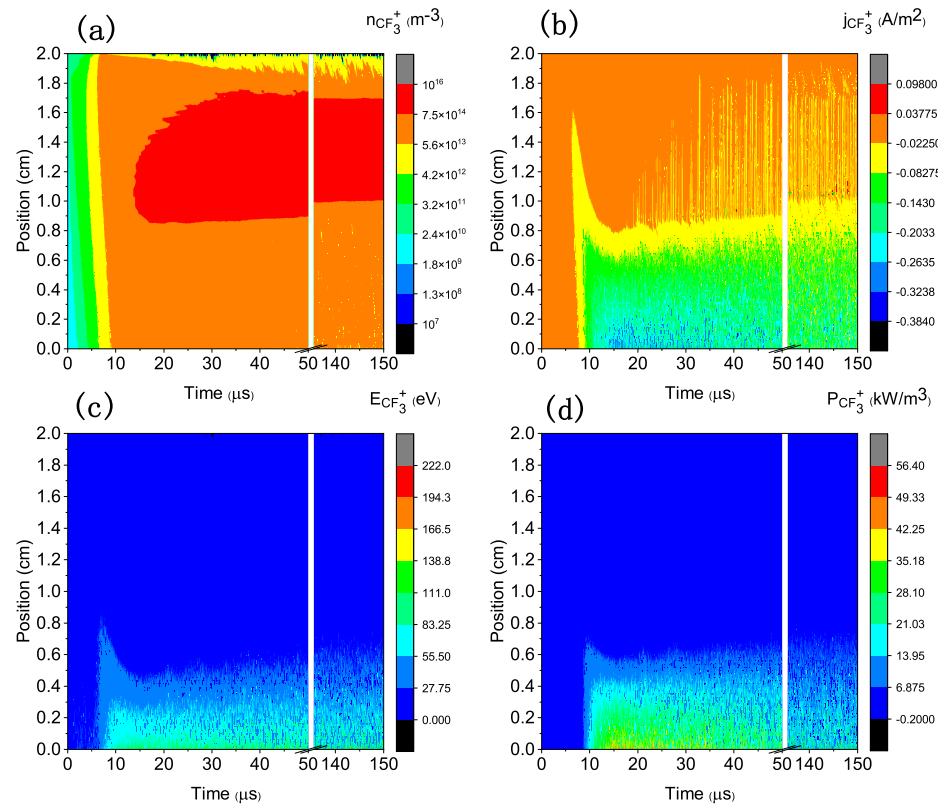**Figure 5.** Spatiotemporal distribution of (**a**) I^+ density, (**b**) I^+ current density, (**c**) average I^+ energy, (**d**) I^+ heating rate.

Figure 6. Spatiotemporal distribution of (**a**) CF_3^+ density, (**b**) CF_3^+ current density, (**c**) average CF_3^+ energy, (**d**) CF_3^+ heating rate.
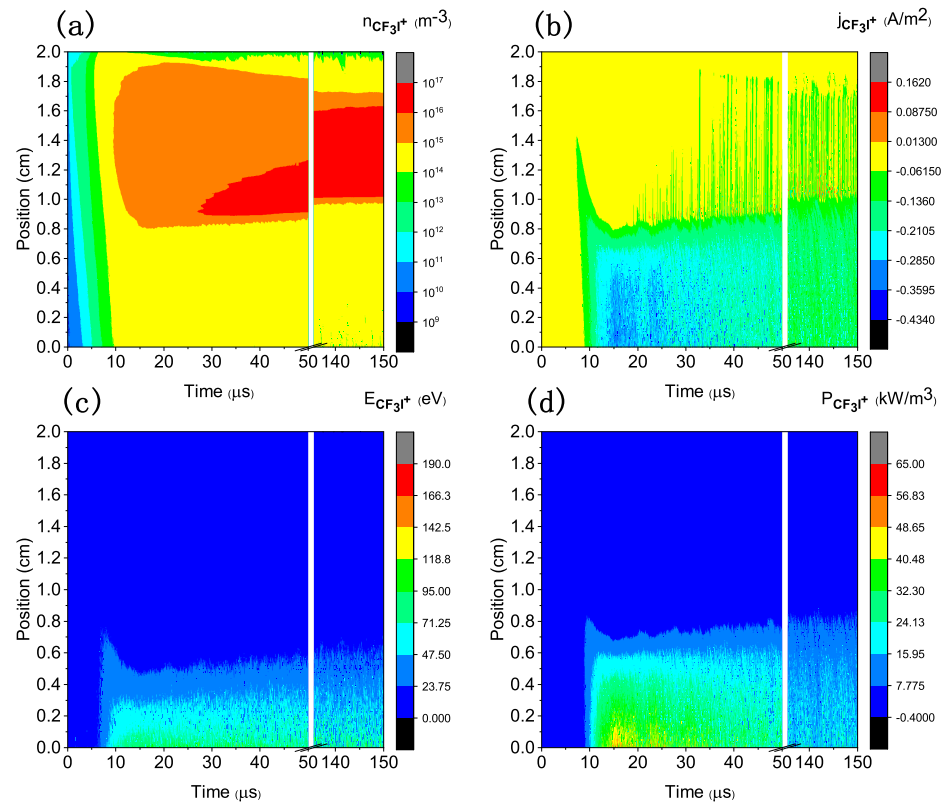
Figure 7. Spatiotemporal distribution of (**a**) CF_3I^+ density, (**b**) CF_3I^+ current density, (**c**) average CF_3I^+ energy, (**d**) CF_3I^+ heating rate.
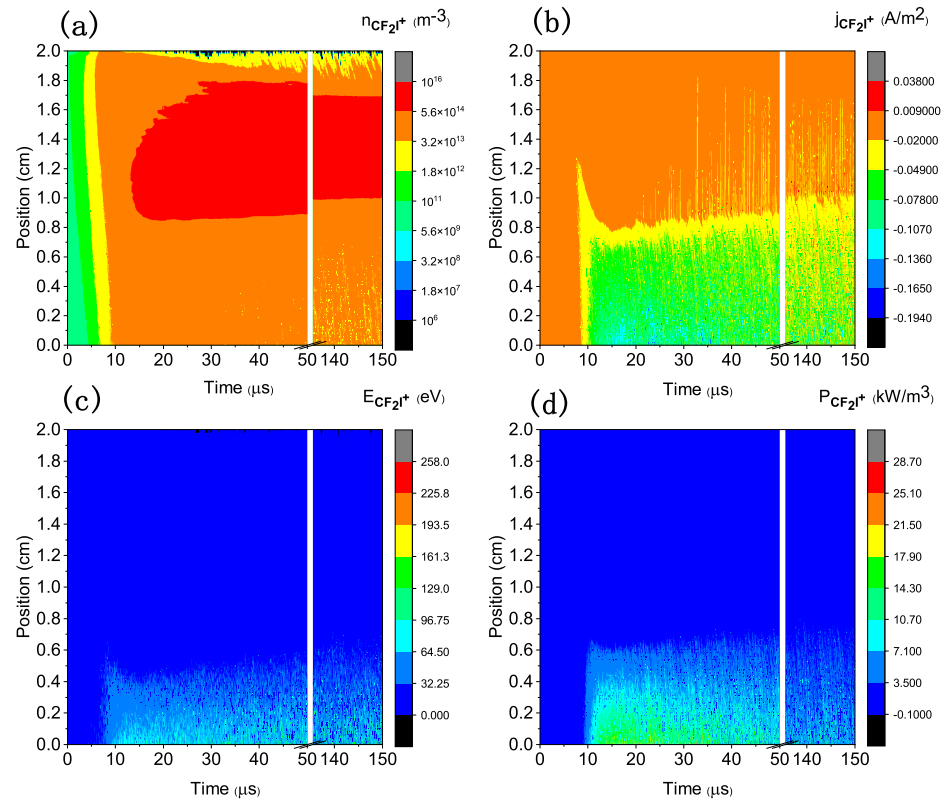
Figure 8. Spatiotemporal distribution of (**a**) CF_2I^+ density, (**b**) CF_2I^+ current density, (**c**) average CF_2I^+ energy, (**d**) CF_2I^+ heating rate.

During the before-breakdown stage, positive ions exhibit distinct characteristics compared to electrons and negative ions. In the presence of an electric field, positive ions migrate from the anode to the cathode. Unlike electrons, the density of positive ions does not initially decrease but continues to rise steadily, as depicted in Figures 5a–8a. This phenomenon arises because all positive ions involved in the reaction are heavy ions, resulting in significantly lower ion mobility compared to electrons. Consequently, positive ions near the cathode are not lost as rapidly as electrons. In contrast to negative ions, positive ions are more evenly distributed. This occurs as positive ions gradually approach the cathode under the influence of the electric field, leading to an increase in positive ion density near the cathode. As previously mentioned, electrons accelerate from the cathode to the anode under the influence of the electric field. Closer proximity to the anode results in higher electron energy, increasing the likelihood of ionization reactions. Ionization reactions generate a substantial number of positive ions. Therefore, despite a portion of positive ions gradually moving toward the cathode from the anode due to the electric field, the vigorous ionization reactions near the anode replenish the depleted positive ion density, preventing the density near the anode from dropping to zero. During the before-breakdown stage, the density of I^+ near the anode increases to 10^{11} m^{-3}, while near the cathode, it rises to 10^{14} m^{-3}, resulting in an overall average density elevation to 10^{13} m^{-3}. Similar density distributions are observed for CF_3^+, CF_3I^+, and CF_2I^+, with higher densities near the anode. Although the density of positive ions during the before-breakdown stage has increased compared to the initial density of 5×10^9 m^{-3}, it remains relatively low compared to the breakdown stage. Consequently, the current density and heating rate of positive ions during this stage are substantially lower than during the breakdown stage. For instance, considering I^+, its current density before breakdown consistently remains below 1 Am^{-2}, with a heating rate also below 1 kWm^{-3}. Similar current densities and heating rates are observed for CF_3^+, CF_3I^+, and CF_2I^+.

During the breakdown stage, the intense ionization reaction triggers a rapid surge in positive ion density. In the bulk region, the density of I^+ sharply rises to 2.5×10^{15} m^{-3}, while within the cathode sheath, it reaches 10^{14} m^{-3}, resulting in an overall average density of 10^{15} m^{-3}. Similar trends are observed for CF_3^+, CF_3I^+, and CF_2I^+. Notably, the densities of I^+ and CF_3I^+ tend to surpass those of CF_3^+ and CF_2I^+ during the breakdown stage due to slightly higher ionization reaction cross-sections. The densities of all four positive ions significantly escalate during the breakdown stage, both within the bulk region and the cathode sheath. Notably, the density of positive ions in the bulk region is approximately one order of magnitude higher than that in the cathode sheath. However, a reverse trend is observed for energy, heating rate, and current density. The strong electric field within the cathode sheath accelerates positive ions, resulting in higher energy, heating rate, and current density compared to the bulk region. For instance, for I^+, the energy in the bulk region is less than 1 eV, while within the sheath, it elevates to 60 eV. Similarly, for CF_3^+, CF_3I^+, and CF_2I^+, the energy in the sheath surpasses that of the bulk region. Ultimately, higher positive ion current densities (I^+ is -0.2 Am^{-2}, CF_3^+ is -0.2 Am^{-2}, CF_3I^+ is -0.25 Am^{-2}, CF_2I^+ is -0.1 Am^{-2}) and stronger ion heating rates (I^+ is 30 kWm^{-3}, CF_3^+ is 35 kWm^{-3}, CF_3I^+ is 35 kWm^{-3}, CF_2I^+ is 10 kWm^{-3}) manifest in the cathode sheath. Despite the higher density of positive ions in the bulk region, the energy, current density, and heating rate are notably lower compared to those in the cathode sheath due to the electric field shielding effect.

In the after-breakdown stage, depicted in Figures 5a–8a, the density of positive ions within the bulk region continues to ascend gradually. The densities of I^+, CF_3^+, CF_3I^+, and CF_2I^+ within the bulk region all steadily increase to approximately 10^{16} m^{-3}. In contrast, the density within the cathode sheath remains around 10^{14} m^{-3}, while near the anode, it diminishes further to approximately 10^{13} m^{-3}.

3.4. Negative Ion Kinetics

The negative ion considered in this paper is I^-. The spatial and temporal distributions of negative ions are shown in Figure 9.
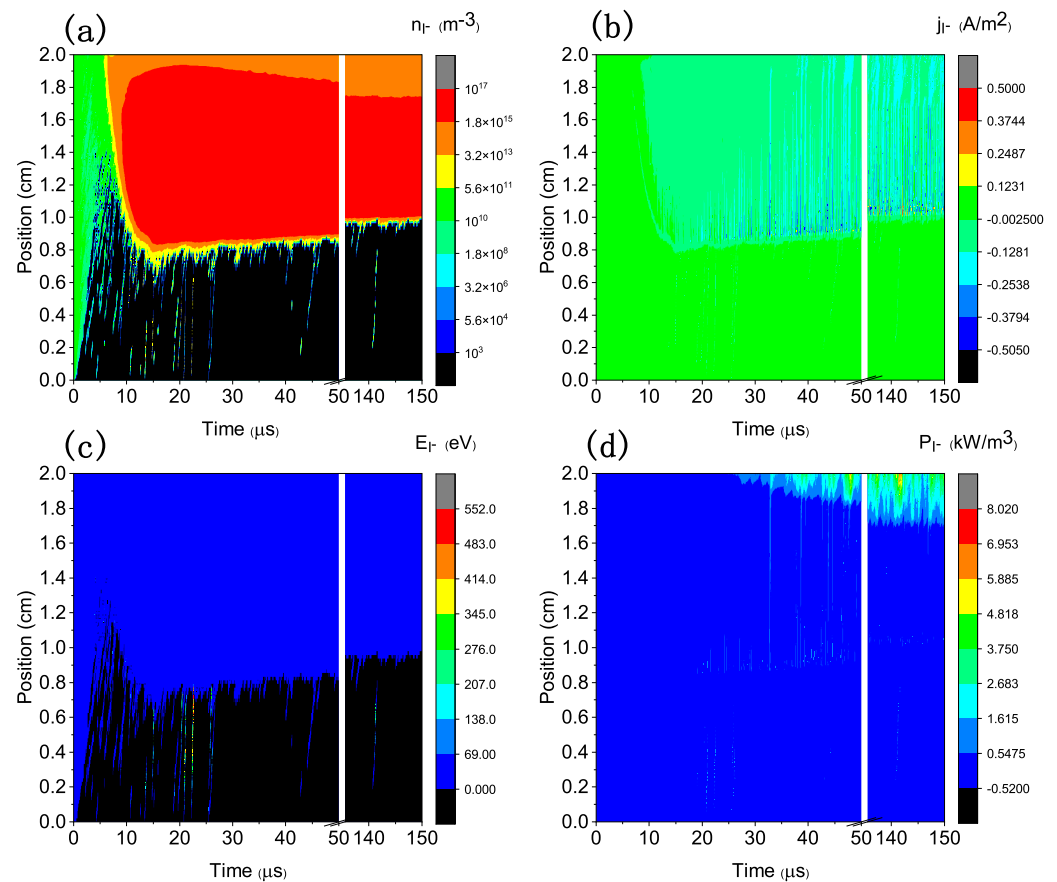

Figure 9. Spatiotemporal distribution of (**a**) I^- density, (**b**) I^- current density, (**c**) average I^- energy, (**d**) I^- heating rate.

In the before-breakdown stage, negative ions migrate from the cathode toward the anode under the influence of the electric field, increasing the density of I^- near the anode. However, as the I^- near the cathode is not replenished, its density gradually diminishes. Notably, the spatial distribution of negative ions appears less uniform compared to positive ions. By approximately 6.4 μs, the I^- density near the cathode approaches zero, while near the anode, it elevates to 10^{12} m^{-3}, yielding an average density of 3×10^{11} m^{-3} at this juncture. It's evident that the density of I^- in the before-breakdown stage only increases by one order of magnitude, which is substantially smaller compared to the increments observed for electrons and positive ions. The energy of I^- escalates as it approaches the anode due to the accelerating effect of the electric field, reaching approximately 15 eV near the anode, while remaining below 1 eV near the cathode. Moreover, the heating rate and current density of I^- are notably lower compared to positive ions and electrons. This disparity can be attributed to the heavy mass, low mobility, and lower spatial density of I^- relative to electrons and positive ions.

During the breakdown stage, the density of I^- in the bulk region experiences a rapid escalation from 10^{12} m^{-3} to nearly 10^{16} m^{-3}. In contrast, the density of I^- in the cathode sheath remains extremely low, approaching zero. This disparity arises from the propensity of electrons with lower energies to induce adsorption reactions, while those in the cathode sheath, characterized by significantly higher energies, predominantly undergo ionization reactions. Consequently, there is minimal addition of new I^- in the cathode sheath, leading to continuous consumption and limited replenishment, resulting in a much lower density

compared to the bulk region. However, the average density of I^- increases substantially to 4×10^{15} m^{-3}, marking a four-order-of-magnitude increase relative to the before-breakdown stage. The extremely low density of I^- in the cathode sheath translates into minimal heating rate and current density values. Although there is a substantial amount of I^- in the bulk region, the shielding effect of the electric field by the sheath layer prevents its acceleration, thus maintaining its energy below 1 eV. Consequently, the heating rate of I^- in the bulk region remains below 1 kWm^{-3}, with a current density of -0.02 Am^{-2}, reflecting the limited influence of I^- in this region.

In the after-breakdown stage, the higher energy of electrons in the anode sheath compared to those in the bulk reduces the probability of adsorption reactions, leading to the depletion of I^- in the anode sheath. This results in an I^- density of 10^{14} m^{-3} in the anode sheath, which is much lower than 10^{16} m^{-3} in the bulk region.

In the stable phase after the formation of the anode sheath, each parameter remains basically constant. However, because of the existence of an electric field in the anode sheath, the current density and heating rate of I^- are significantly higher than those of the bulk region. For example, the heating rate of the anode sheath is 2.6 kWm^{-3}, while that of the bulk region is only 0.05 kWm^{-3}. In contrast, the electric field in the cathode sheath is strong, but the heating rate and current density are close to zero due to the low density of I^-.

3.5. Electrical Characteristics

To study the electrical characteristics of plasma breakdown, the voltage, current, potential between plates, and the electric field of the external circuit are also diagnosed in the simulation process. Figure 10 shows the voltage and current images throughout the breakdown process.
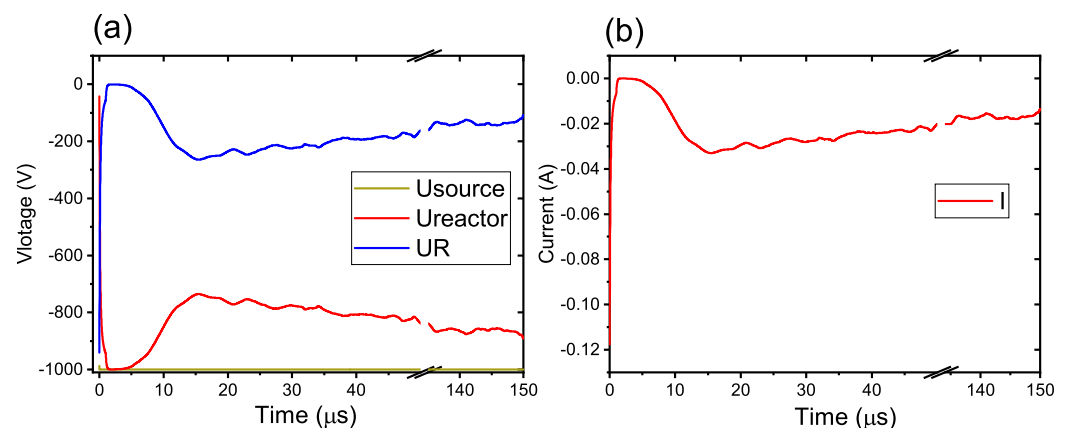

Figure 10. Time curves of (**a**) voltage (V) , (**b**) current (A).

In the before-breakdown stage, the electric field can freely penetrate the entire plate space, resulting in a uniform electric field between the plates, similar to a capacitor. Figure 10a shows the voltage ($U_{reactor}$) applied between the two plates increases rapidly from the initial value of 0 V to a maximum value of 1000 V, set by the voltage source. The potential of the discharge area between the positive and negative plates decreases from -1000 V of the anode to 0 of the ground cathode with the same gradient, and the electric field intensity is -50 kV/m, as calculated. Before the breakdown, Figure 10b shows that the current in the circuit is almost 0.

During the breakdown stage, the cathode sheath shields the electric field in the bulk region, resulting in a strong electric field at the cathode sheath. The voltage drops are concentrated in the cathode sheath, which can be modeled as an RC circuit. As the gas gradually breaks down, the plate can be represented as a resistive device, evidenced by the presence of current in the circuit, with the resistor sharing a portion of the voltage.

In the after-breakdown stage, the parameters gradually stabilized and the current was approximately -0.017 A. The voltage across the resistor was 150 V and the plate voltage

was 850 V. The equivalent resistance of the plasma was calculated to be approximately 3.5 kΩ. The anode sheath formed after 15 μs and its thickness was stabilized at 0.3 cm. The intensity of the internal electric field ranged from −2 kV/m to 30 kV/m as the plasma stabilized.

4. Discussions

4.1. Particle Kinetics

The previous sections have completely discussed the dynamics of particles. This section analyzes the whole breakdown process from the perspective of particle balance. To better explain the mechanism of the whole breakdown process, this section selects several representative moments from three stages: 1 μs time, corresponding to the before-breakdown stage; 6.4 μs, corresponding to the starting time of the breakdown stage; 10 μs, corresponding to breakdown stage; 15 μs, corresponding to the end of the breakdown stage; 25 μs, corresponding to the anode sheath formation phase in the after-breakdown stage; and 150 μs, corresponding to the stable phase in the after-breakdown stage.

The instantaneous distributions of the electron, negative ion, and positive ion densities, energies, current densities, and space potentials are presented in Figures 11, 12, 13, and 14, respectively.
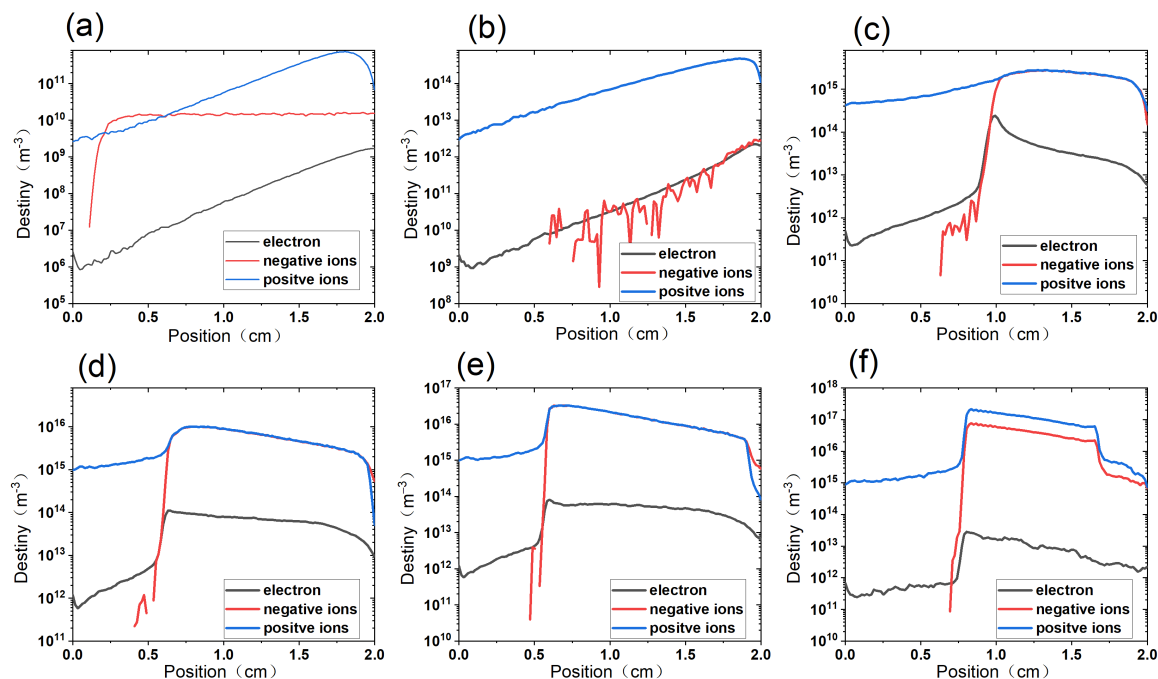

Figure 11. Density snapshots at (**a**) 1 μs, (**b**) 6.4 μs, (**c**) 10 μs, (**d**) 15 μs, (**e**) 25 μs, and (**f**) 150 μs.

In the before-breakdown stage, the overall electron density is low, ranging between 10^8 m^{-3} and 10^{10} m^{-3} at each location, allowing the external electric field to permeate the entire discharge gap. As depicted in Figure 14a, the electric field between the electrodes is uniformly distributed, as evidenced by the potential difference between them. The density and energy of the electron are used to compute the Debye length, estimated at approximately 5.4 m, significantly exceeding the inter-electrode spacing. This confirms the confinement of the entire discharge region within the electric field. Since the electric field in the before-breakdown stage remains unshielded, particles between the electrodes experience acceleration, resulting in a substantial increase in their energies. Under the influence of the electric field, positive ions migrate from the anode to the cathode, resulting in higher energy positive ions near the cathode location. The exact opposite is true for electrons and negative ions. The overall energy of positive ions surpasses that of negative ions and electrons because of their higher density. Ions, having greater mass and lower

mobility compared to electrons, exhibit a more uniform density distribution. Because of their high velocity, the electron density increases closer to the anode, while decreasing closer to the cathode. However, in Figure 14a, a "paradoxical" increase in the electron density is observed at the cathode, attributed to positive ions on the cathode plate causing a secondary electron emission effect, thus slightly elevating the electron density near the cathode. As depicted in Figure 13a, both electrons and negative ions exhibit a higher current density near the anode, whereas positive ions exhibit a larger current density at the cathode. In general, particle energy, current density, and other parameters in the before-breakdown stage are significantly low.
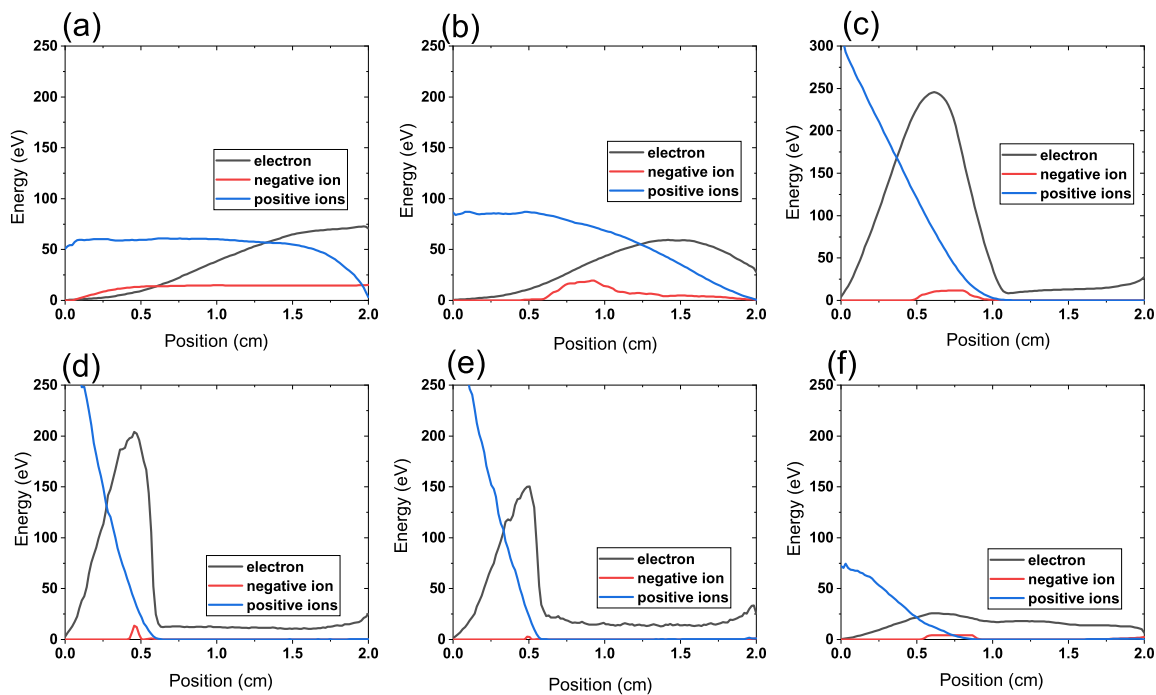

Figure 12. Energy snapshots at (**a**) 1 μs (before breakdown), (**b**) 6.4 μs (breakdown), (**c**) 10 μs (breakdown), (**d**) 15 μs (breakdown), (**e**) 25 μs (anode sheath formation phase of after breakdown), and (**f**) 150 μs (stable phase of after breakdown).

The breakdown stage begins at 6.4 μs, and the transient distributions at this point are specifically highlighted in this paper, as shown in the (b) plots of Figures 11–14. During this phase, the collision of high-energy electrons with the background gas primarily instigates ionization reactions. The newly generated electrons from these reactions are then accelerated by the electric field, further initiating additional ionization reactions, leading to a rapid surge in the electron density, known as electron avalanche. In this process, not only does the electron density increase dramatically, but the density of positive ions also experiences a significant upsurge. A comparison between Figure 11a,b reveals that the density of positive ions and electrons during the breakdown process increases by two orders of magnitude compared to the before-breakdown stage. Both negative ions and electrons migrate from the cathode toward the anode, causing a reduction in the density of negative ions and electrons near the cathode. As positive ions collide with the cathode, producing secondary electrons that replenish some of the quantity lost by electron drift toward the anode, the density of negative ions at the cathode is consequently lower than that of electrons. With an increase in particle density, the current density experiences a significant surge. Comparing Figure 13a with Figure 13b, the absolute value of the electron current density near the positive plate increases significantly, from approximately 0.01 Am^{-2} to 0.45 Am^{-2}. In Figure 14b, the potential near the plate changes from -1000 V to -990 V. This change is attributed to the progressive increase in current between plates with the onset of the breakdown process, resulting in a higher current in the external circuit.

Consequently, this causes the partial voltage across the external resistor to increase, leading to a reduction in the absolute value of the voltage between the pole plates to less than 1000 V.
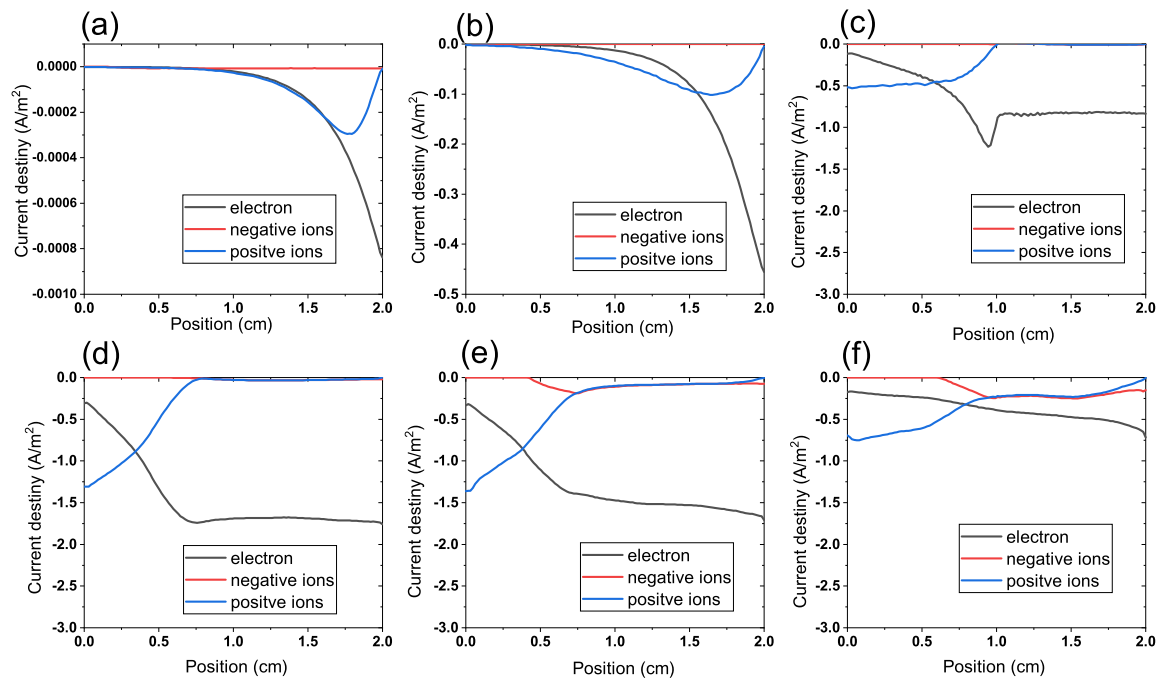

Figure 13. Current density snapshots at (**a**) 1 μs, (**b**) 6.4 μs, (**c**) 10 μs, (**d**) 15 μs, (**e**) 25 μs, and (**f**) 150 μs.
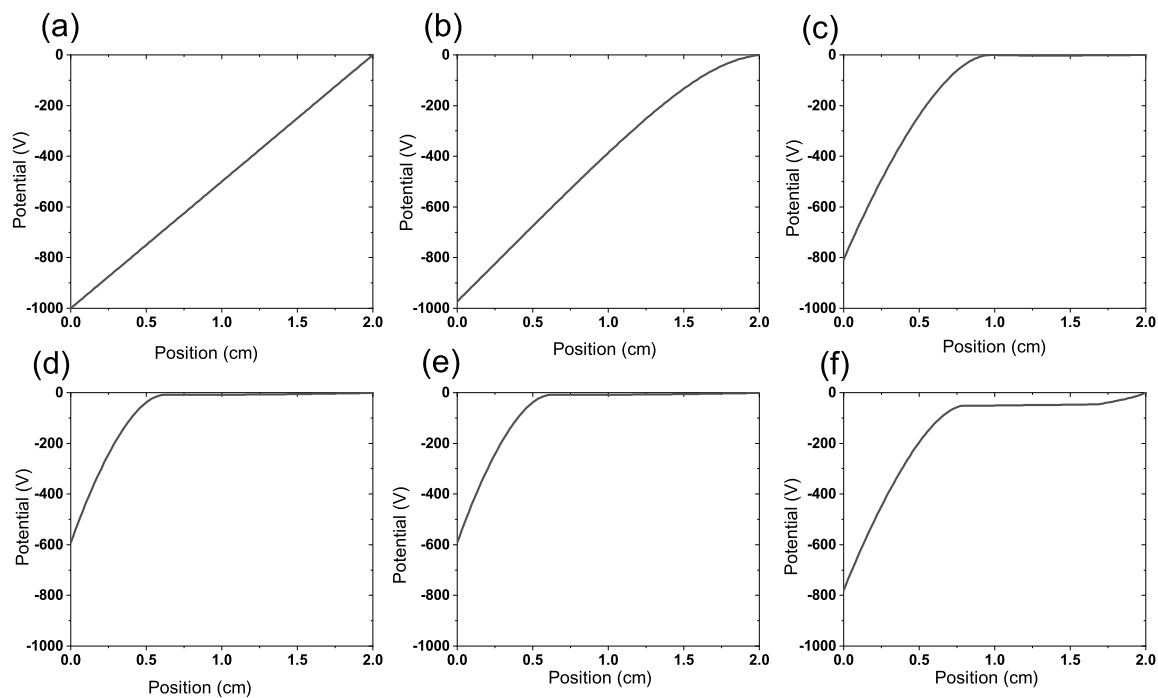
Figure 14. Potential snapshots at (**a**) 1 μs, (**b**) 6.4 μs, (**c**) 10 μs, (**d**) 15 μs, (**e**) 25 μs, and (**f**) 150 μs.

At 10 μs, the breakdown process enters an intermediate stage, during which the cathode sheath gradually forms, as illustrated in Figures 11c–14c. The density of positive ions near the cathode surpasses that of electrons and negative ions, resulting in a positive net charge near the cathode. This uneven distribution of space charge generates an electric field directed toward the anode, which shields the applied electric field. Consequently, the strength of the electric field diminishes in the anode region, causing electrons to

decelerate and rapidly lose energy. Simultaneously, this phenomenon leads to an escalation in the electric field near the cathode, resulting in an increased energy of electrons within the cathode sheath. As depicted in Figure 12c, the electron energy in the anode region measures approximately 15 eV, while high-energy electrons of around 350 eV emerge in the cathode sheath. When comparing Figures 11c and 12c, it is evident that while the electron density in the anode region exceeds that of the cathode region by two orders of magnitude, the electron energy in the anode region is significantly lower than that in the cathode region. The combination of high-density, low-energy electrons in the anode region results in a more vigorous adsorption reaction in comparison to ionization reactions. Consequently, this leads to the generation of a substantial number of negative ions in the anode region. In contrast, the cathode region lacks replenishment of negative ions, with its negative ion density nearing zero. Consequently, the electric field generated by the uneven distribution of the charge continues to intensify, gradually expanding the cathode sheath. In Figure 14c, the potential near the anode approaches zero due to the shielding effect of the electric field, while the potential of the cathode plate measures −930 V. It should be noted that the absolute voltage value between the plates is lower than that at 6.4 μs, due to the ongoing increase in current between the plates. This observation is further supported by comparing the current densities in Figure 13b with Figure 13c, revealing a significant increase in the current density.

At 15 μs, the breakdown stage is complete and a stable cathode sheath has been formed, as evidenced by the images in Figures 11d and 14d. As shown in Figure 11d, the positive ion density curve in the bulk region coincides with the negative ion density curve. Figure 12d reveals that the energy of positive and negative ions and electrons in the bulk region is small, while a large energy is obtained in the cathode sheath. This is because the electric field in the bulk region is almost zero. However, the strong electric field in the sheath is opposite to that in the bulk region. Figure 14d shows that the potential of the bulk region is close to 0, indicating that the bulk region is electrically neutral.

The formation phase of the anode sheath in the after-breakdown stage is observed at 25 μs, as shown in Figures 11e–14e. The recombination process causes a rapid increase in the positive ion density, resulting in a change in the electric field shielding near the anode and the formation of the anode sheath.

The stable phase in the after-breakdown stage is observed at 150 μs, as shown in Figures 11f–14f. The left side of the figure is the cathode sheath, the middle bulk region has the highest density, and the right side is the thin anode sheath. The electric field accelerates the positive ions in the cathode sheath to higher energies.

4.2. Power Balance

The energy conservation of the discharge process is important to consider. Two primary sources of energy for particles are the electric field between the plates, known as the heating effect, and the secondary electron emission effect induced by the impact of ions on the plate. Two energy loss terms must also be taken into account: particles absorbed by the plate at the boundary and particles dissipating energy through collision with one another.

In the DC discharge process, the change value of the total kinetic energy (dE_k/dt) of all particles is typically too small to be compared to other power terms. Consequently, the energy conservation principle can be employed to derive the power balance equation of the discharge device as follows:

$$P_{\text{heating}} + P_{SEE} = P_{\text{collision}} + P_{\text{boundary}} \tag{3}$$

Among them, P_{heating} is the heating power, which is the main production term of the particle energy:

$$P_{\text{heating}} = \int E \cdot (j_e + j_i) \tag{4}$$

Among them, E is the intensity of the electric field, j_e is the electron current density, and j_i is the ion current density. This algorithm obtains the heating power of each position in the discharge space by diagnosing the electric field intensity, electron current density, and ion current density of each position in the discharge space and then integrates the heating power of each position in the discharge space to obtain the heating power.

P_{SEE} is the secondary electron emission (*SEE*) power, another term for small energy production:

$$P_{SEE} = \frac{E_{SEE}}{dt} \tag{5}$$

Among them, E_{SEE} is the total energy of secondary electrons emitted by the electrode in unit time, which can be obtained by counting the number and energy of secondary electrons.

$P_{\text{collision}}$ is collision loss power, which is lost through particle collisions:

$$P_{\text{collision}} = \frac{E_{\text{beforeMCC}} - E_{\text{aferMCC}}}{dt} \tag{6}$$

Among them, $E_{\text{beforeMCC}}$ and E_{afterMCC} are the total particle energies before and after the Monte Carlo collision (MCC), respectively.

P_{boundary} is the boundary loss power, which is the power absorbed by the boundary when the particles move to the boundary:

$$P_{\text{boundary}} = \frac{E_{\text{boundary}}}{dt} \tag{7}$$

Among them, E_{boundary} is the total energy of all particles bombarded with the plate in unit time, and the boundary loss power is obtained by dividing the total energy of all particles bombarded with the plate in unit time by unit time. Because the heating power of electrons is of special research significance, this paper divides the heating power into the electronic heating power P_{eheating} and the ion heating power P_{iheating}. The corresponding equations are as follows:

$$P_{\text{heating}} = P_{\text{eheating}} + P_{\text{iheating}} \tag{8}$$

$$P_{\text{eheating}} = P_{\text{ecollision}} + P_{\text{eboundary}} - P_{SEE} \tag{9}$$

$$P_{\text{iheating}} = P_{\text{icollision}} + P_{\text{iboundary}} \tag{10}$$

where $P_{\text{ecollision}}$ is the electron collision loss power, $P_{\text{eboundary}}$ is electron boundary loss power, $P_{\text{icollision}}$ is ion collision loss power, and $P_{\text{iboundary}}$ is ion boundary loss power.

The power balance in a discharge process can be studied by diagnostically calculating the total, electron, negative ion, and positive ion powers according to the appropriate equations. Figure 15 shows these powers, with (a) representing the total power balance, (b) the electron power balance, (c) the negative ion power balance, and (d) the positive ion power balance. The analysis and verification of the power balance in the discharge process can be carried out using these data.

In order to reduce the noise of the simulated data, the adjacent average method was employed to smooth the curves, using 200 window points. Because the secondary electron emission power is too small compared to the other powers, it was displayed separately with a smaller Y-axis to avoid coinciding with the X-axis in the conventional coordinate range display.

In the before-breakdown stage (0–6.4 µs), the number of particles is too low and the reaction is not intense enough, resulting in low power terms for each particle as shown in Figure 15, with values close to 0. Consequently, further discussion of this stage is unnecessary.
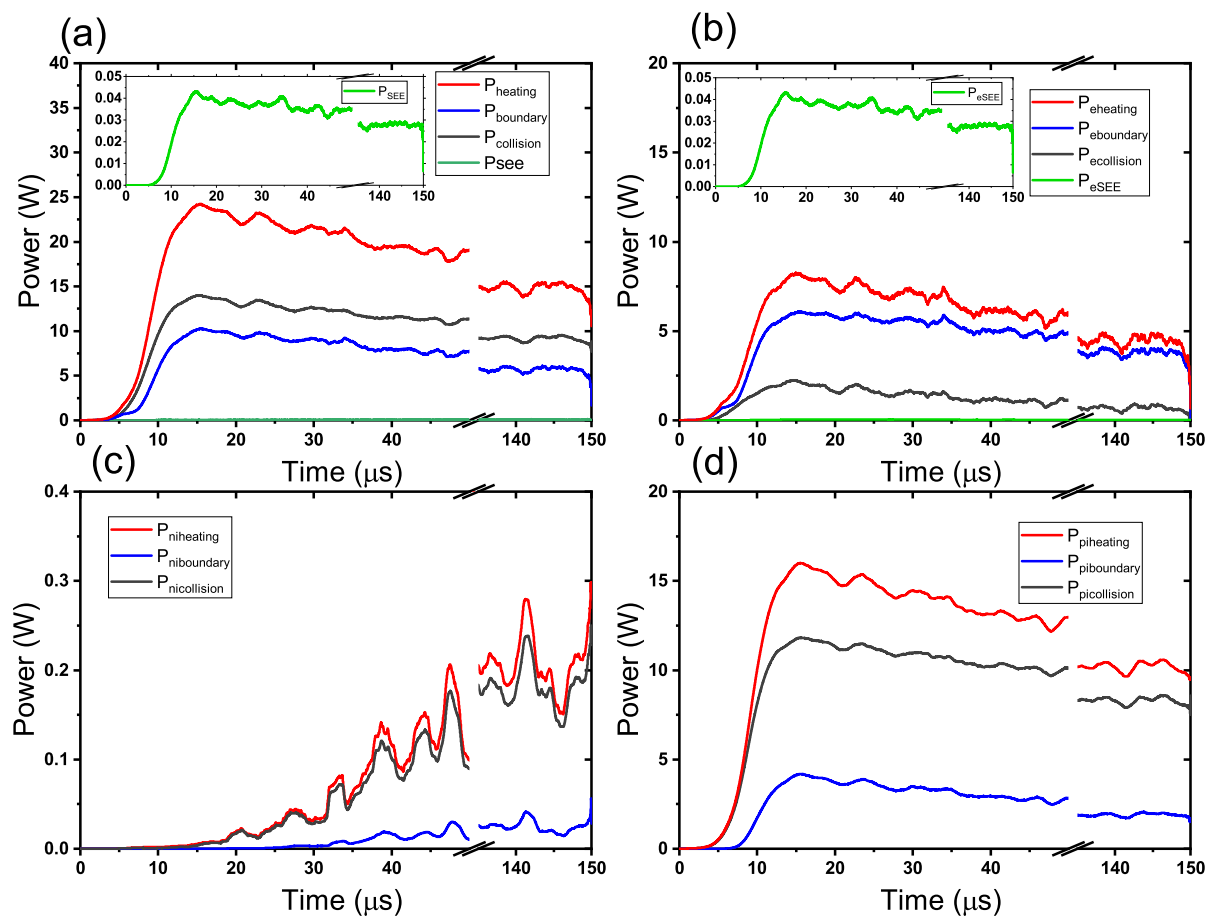
Figure 15. Power balance of (**a**) sum, (**b**) electron, (**c**) negative ions, (**d**) positive ions (Smoothed).

During the breakdown stage (6.4–15 µs), the power related to electrons and positive ions increases sharply. The electron density is smaller than the positive ion density, resulting in a lower growth rate for the electron-related power compared to the positive ion-related power, as shown in Table 1. The secondary electron emission power is observed to have a negligible effect, as seen in Figure 15a,b. The exponential growth of positive ion density and the violent ionization reaction lead to a significant increase in the heating power of positive ions, as shown in Figure 15d. The heating power associated with negative ions remains relatively constant, as the number of particles, energy, and current associated with negative ions is comparatively small, resulting in a correspondingly small heating power, as seen in Figures 11, 12b,c and 13.

In the after-breakdown stage (15–150 µs), the plasma enters a stable state, and the power associated with each particle gradually decreases, reaching a dynamic equilibrium state, consistent with previous observations. Positive ions contribute the most to the heating power, accounting for approximately 62% of the total. Negative ions exhibit a small proportion of heating power, around 1.5%. The power loss of electrons is mainly due to boundary losses, accounting for approximately 85% of the total losses. The remaining losses come from collision losses. On the other hand, for ions, the ratio of the boundary loss power drops below 40%, and most of the power absorbed by the ions is dissipated through the elastic collision and recombination process due to their larger mass and lower mobility, leading to a smaller number of ions bombarding the plate.

4.3. Paschen Curve

The Paschen curve, which is derived from a model based on an analytical fit of the first ionization Townsend coefficient, describes the breakdown voltage of a gas U_b as a function of pressure P and gap distance between electrodes d:

$$U_b = f(Pd) \tag{11}$$

By systematically scanning a wide range of parameters for CF_3I, we calculated and compared the Paschen curves of CF_3I and SF_6, as shown in Figure 16. This comparative analysis facilitates a comprehensive evaluation of the breakdown characteristics of CF_3I and SF_6 at low pressures [21].
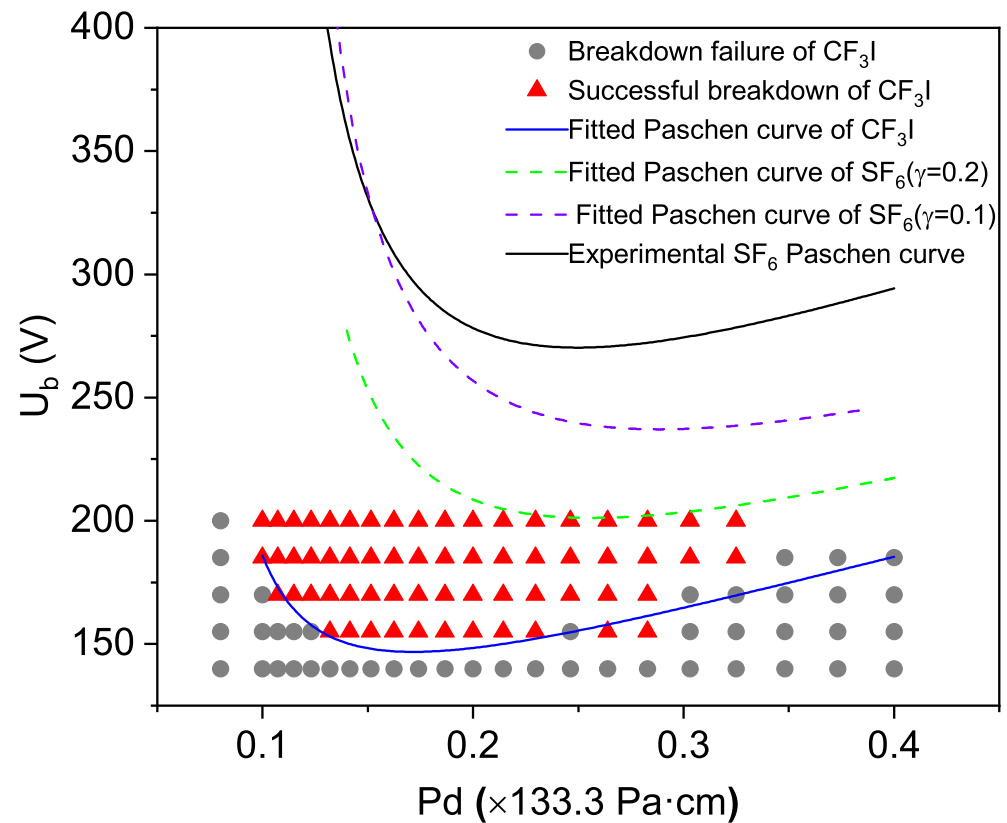

Figure 16. Paschen curve of trifluoroiodomethane and sulfur hexafluoride [21].

The red and gray dots represent successful and unsuccessful breakdown points, respectively, under these conditions. The blue curve represents the theoretical Paschen curve of CF_3I with a secondary electron emission coefficient of 0.2. Meanwhile, the green and purple curves represent the theoretical Paschen curves of SF_6 with secondary electron emission coefficients of 0.2 and 0.1, respectively. The black curve corresponds to the experimentally obtained Paschen curve of SF_6.

The horizontal axis of the Paschen curve is the product of pressure and the gap distance Pd, and the unit is generally ×133.3 Pa·cm. This conversion is because the pressure unit used in the simulation program is Torr and 1 Torr = 133.3 Pa, so after multiplying the distance between the two, the unit becomes Torr · cm. The breakdown voltage of the gas gap on the longitudinal axis is Ub and the unit is V.

In a uniform electric field, the Paschen curve of the gas is generally "U" shaped, that is, there is a point at which the breakdown voltage reaches a minimum. It is evident that the simulated Paschen curves align perfectly with the characteristic "U" shape.

For the CF_3I parameter scan, a fixed secondary electron emission coefficient of 0.2 was used. In contrast, during the SF_6 Paschen curve investigation, two cases were considered, which incorporated secondary electron emission coefficients of 0.1 and 0.2, respectively. These cases were juxtaposed with experimental measurements of the SF_6 Paschen curves, revealing a significant influence of the secondary electron emission coefficient on the Paschen curves. This suggests that the experimental measurements for the SF_6 Paschen

curves were conducted using a material with a secondary electron emission coefficient of approximately 0.1.

Unfortunately, the parameters for the Paschen curve of CF$_3$I at low pressures could not be obtained. However, through a comparative analysis with the Paschen curve of SF$_6$ at low pressures, we assert the reliability of our results.

As illustrated in Figure 16, under low-pressure conditions, CF$_3$I demonstrates a lower breakdown voltage compared to SF$_6$. Under high pressure conditions, the breakdown voltage of pure CF$_3$I has been shown to exceed that of SF$_6$ [44,45]. However, experiments also indicate that under low-pressure conditions, the breakdown voltage of CF$_3$I may be lower than that of SF$_6$, attributable to CF$_3$I's heightened sensitivity to changes in the electric field [46]. Therefore, the results of this article are consistent with the experiments qualitatively.

In addition, according to the formula for calculating the Paschen curve (12), when *A*, *B*, γ_{se} are determined, the fitted Paschen curve can be obtained, as follows:

$$U_b = f(Pd) = \frac{Bpd}{\ln Apd - \ln[\ln(1 + 1/\gamma_{se})]} \tag{12}$$

Among them, *A* and *B* are determined by experiments that depend on the constants of gas properties. γ_{se} is the average value of the secondary electron emission. According to the previous text, this paper sets it to 0.2. *A*, and the value of *B* is shown in Table 2. The Paschen curve is related to the electrode material, and when the electrode material changes, the secondary electron emission coefficient also changes.

Table 2. Constants of the Equation.

Gas	A (cm^{-1}mTorr^{-1})	B (Vcm^{-1}mTorr^{-1})
CF$_3$I	0.0316	0.9842
SF$_6$	0.0171	0.7863

5. Conclusions

This paper employs a one-dimensional implicit PIC/MCC model to investigate the evolution process of pure CF$_3$I gas under the low-pressure direct current and, based on this, plots the Paschen curve of CF$_3$I.

The whole process is distinguished as before-breakdown, breakdown, and after-breakdown stages. In this paper, changes in the particle density, current density, and particle energy of electrons, positive ions, and negative ions in each stage of the breakdown process are studied in depth. In addition, this paper analyzes the particle balance and power balance throughout the process, thus providing insight into how particles are generated and lost at each stage, as well as the power source and loss terms for each particle. The results of this paper show that the successful breakdown mode is characterized by a sharp increase in the number of particles and a corresponding increase in the power associated with electrons, positive ions, and negative ions.

In addition, this paper studies the Paschen curve of CF$_3$I and compares it with that of SF$_6$. The results suggest that while CF$_3$I is an environmentally friendly alternative to SF$_6$, it may not be suitable for use in low-pressure applications due to its inferior insulation characteristics in some cases. Further research is needed to determine the suitability of CF$_3$I for use in other applications. In the future, our study will explore interesting directions by comparing the insulation characteristics of pure CF$_3$I and SF$_6$ under higher pressure conditions, as well as analyzing the breakdown characteristics of pure CF$_3$I and CF$_3$I gas mixtures. These investigations are of particular interest in the fields of dielectrics and electrical insulation.

Abbreviations

The following abbreviations are used in this manuscript:

PIC/MCC	particle-unit/Monte Carlo collision
GWP	global warming potential
SF_6	sulfur hexafluoride
CF_3I	trifluoroiodomethane
DF	dual frequency
CCP	capacitively coupled plasma
SEE	secondary electron emission

Appendix A. Collision Reactions List

According to the LXCAT database [24], 12 electron—molecule collision reactions are listed in Table A1.

There are 614 ion–molecule collision reactions considered in the model, and the corresponding thermodynamic threshold energies are calculated based on the dissociation energy of the molecule, electron affinity, and ionization energy. Tables A2–A6 present several typical reactions of the $I^- - CF_3I$, $CF_3^+ - CF_3I$, $I^- - CF_3I$, $CF_2I^+ - CF_3I$, $CF_3I^+ - CF_3I$ collisions, respectively.

Table A1. e + CF_3I reactions and the threshold energies Δ E.

No.	e + $CF_3I \rightarrow$	Δ E (eV)
1	$I^- + CF_3$	0.000000×10^0
2	$e + CF_3I$	0.000000×10^0
3	$e + CF_3I(v)$	1.400000×10^{-1}
4	$e + CF_3I(e_1)$	4.700000×10^0
5	$e + CF_3I(e_2)$	7.200000×10^0
6	$e + CF_3I(e_3)$	8.100000×10^0
7	$e + CF_3I(e_4)$	9.000000×10^0
8	$e + CF_3I(e_5)$	9.800000×10^0
9	$e + e + CF_3I^+$	1.023000×10^1
10	$e + e + CF_3^+ + I$	1.100000×10^1
11	$e + e + CF_2I^+ + F$	1.200000×10^1
12	$e + e + CF_3 + I^+$	1.300000×10^1

Table A2. $I^- + CF_3I$ reactions and the threshold energies ΔE.

No.	$I^- + CF_3I \rightarrow$	ΔE (eV)
1	$CF_2I + F + I^-$	5.044
	......	
7	$CF + 2F + I + I^-$	12.584
	......	
17	$C + 2F + F^- + 2I$	17.283
	......	
34	$CF + F_2 + I_2 + e$	12.428

Table A3. $CF_3^+ + CF_3I$ reactions and the threshold energies ΔE.

No.	$CF_3^+ + CF_3I \rightarrow$	ΔE (eV)
1	$CF_3^+ + CF_2I + F$	5.044
	......	
16	$C^+ CF_3I^+ + 3F$	16.162
	......	
32	$C + CF_2I^+ + 2F_2$	17.898
	......	
64	$I^+ + C + CF + 2F_2 + F$	25.645

Table A4. $CF_2I^+ + CF_3I$ reactions and the threshold energies ΔE.

No.	$CF_2I^+ + CF_3I \rightarrow$	ΔE (eV)
1	$CF_2I^+ + CF_2I + F$	5.044
	......	
20	$I^+ + CF_2 + CF_3I$	2.703
	......	
34	$I^+ + 2CF + I + 3F$	20.331
	......	
230	$I^+ + CF_3 + CI + F_2$	11.137

Table A5. $CF_3I^+ + CF_3I$ reactions and the threshold energies ΔE.

No.	$CF_3I^+ + CF_3I \rightarrow$	ΔE (eV)
1	$CF_3I^+ + CF_2I + F$	5.044
	......	
16	$CF_3^+ + I + CF_3I$	1.466
	......	
34	$I^+ + CF_2 + CFI + 3F$	17.835
	......	
110	$I^+ + C + CF + I + 2F_2 + F$	27.111

Table A6. $I^+ + CF_3I$ reactions and the threshold energies ΔE.

No.	$I^+ + CF_3I \rightarrow$	ΔE (eV)
1	$I^+ + CF_2I + F$	5.04 4
	......	
5	$I^+ + C + I + 3F$	17.628
	......	
167	$CF_3^+ + 2I$	1.259
	......	
176	$CF_3^+ + I_2$	-0.311

References

1. Wen, T.; Zhang, Q.; Ma, J.; Guo, C.; You, H.; Qin, Y.; Yin, Y.; Shi, W.; Chen, W. Discharge characteristics of long SF_6 gas gap with and without insulator in GIS under VFTO and LI. *CSEE J. Power Energy Syst.* **2015**, *1*, 16–22. [CrossRef]
2. Christophorou, L.G.; Sauers, I.; James, D.R.; Rodrigo, H.; Pace, M.O.; Carter, J.G.; Hunter, S.R. Recent advances in gaseous dielectrics at Oak Ridge National Laboratory. *IEEE Trans. Electr. Insul.* **1984**, *6*, 550–566. [CrossRef]
3. Katagiri, H.; Kasuya, H.; Mizoguchi, H.; Yanabu, S. Investigation of the performance of CF_3I gas as a possible substitute for SF_6. *IEEE Trans. Dielectr. Electr. Insul.* **2008**, *15*, 1424–1429. [CrossRef]
4. Levko, D.; Raja, L.L. Computational analysis of electrical breakdown of SF_6/N_2 mixtures. *J. Appl. Phys.* **2023**, *133*, 142–149. [CrossRef]
5. Zhou, W.; Zheng, Y.; Yang, S.; Qin, Z.; Wang, B. Research progress and trend of SF_6 alternative with environment friendly insulation gas. *High Volt. Appar.* **2016**, *52*, 8–14.
6. Rabie, M.; Franck, C.M. Comparison of gases for electrical insulation: Fundamental concepts. *IEEE Trans. Dielectr. Electr. Insul.* **2018**, *25*, 649–656. [CrossRef]
7. Solomon, S.; Burkholder, J.B.; Ravishankara, A.R.; Garcia, R.R. Ozone depletion and global warming potentials of CF_3I. *J. Geophys. Res. Atmos.* **1994**, *99*, 20929–20935.
8. Taki, M.; Maekawa, D.; Odaka, H.; Mizoguchi, H.; Yanabu, S. Interruption capability of CF_3I Gas as a substitution candidate for SF_6 gas. *IEEE Trans. Dielectr. Electr. Insul.* **2007**, *14*, 341–346. [CrossRef]
9. Widger, P. *Investigation into CF_3I-CO_2 Gas Mixtures for Insulation of Gas-Insulated Distribution Equipment*; Cardiff University: Cardiff, UK, 2014.
10. Zhao, H.; Li, X.; Jia, S. Calculation of the insulation properties of different CF_3I-N_2 and CF_3I-CO_2 mixtures at 300 K. *High Volt. Eng.* **2013**, *39*, 1692–1697.
11. Zhang, X.; Xiao, S.; Han, Y.; Cressault, Y. Experimental studies on power frequency breakdown voltage of CF_3I/N_2 mixed gas under different electric fields. *Appl. Phys. Lett.* **2016**, *108*, 150–151. [CrossRef]
12. Deng, Y.; Zhao, S.; Yu, J.; Zhang, X.; Zhang, P.; Li, Q.; Li, D. Investigation on the Characteristics of CF_3I Mixtures under Different Conditions. In Proceedings of the 2022 China International Conference on Electricity Distribution (CICED), Changsha, China, 7–8 September 2022.
13. Tu, Y.; Zhou, F.; Wang, C.; Qin, S.; Luo, Y. Discharge breakdown by-products of CF_3I/N_2 gas mixtures at high pressure. In Proceedings of the 2016 IEEE Electrical Insulation Conference (EIC), Montreal, QC, Canada, 19–22 June 2016; Volume 108, pp. 301–304.
14. Cressault, Y.; Connord, V.; Hingana, H.; Teulet, P.; Gleizes, A. Transport properties of CF_3I thermal plasmas mixed with CO_2, air or N_2 as an alternative to SF_6 plasmas in high-voltage circuit breakers. *J. Phys. Appl. Phys.* **2011**, *44*, 49. [CrossRef]
15. Kobayashi, T.; Shioiri, T.; Matsuoka, S.; Kumada, A.; Hidaka, K. Feasibility study of flexible gas-insulated transmission line using CF_3I gas mixture. In Proceedings of the 2020 IEEE 3rd International Conference on Dielectrics (ICD), Valencia, Spain, 5–31 July 2020.
16. Wei, J.; Cruz, A.; Haque, F.; Park, C.; Graber, L. Electrical breakdown characteristics of supercritical trifluoroiodomethane-carbon dioxide (CF_3I-CO_2) mixtures. In Proceedings of the 2020 IEEE Conference on Electrical Insulation and Dielectric Phenomena (CEIDP), East Rutherford, NJ, USA, 18–30 October 2020.
17. Zeng, Q.; Bai, Z.; Liu, W.; He, S.; Zhang, J.; Hu, X.; Miao, G.; Du, X. Etching Performance and Application Research Progress of CF_3I. *Low Temp. Spec. Gases* **2018**, *12*, 160–161.
18. Zhang, J.; Wang, Y.; Duo, L.; Li, G.; Wang, D. Numerical study of He/CF_3I pulsed discharge used to produce iodine atom in chemical oxygen-iodine laser. *Phys. Plasmas* **2013**, *20*, 4. [CrossRef]
19. Hou, J.; Xu, V.; Zhang, K.; Wu, Z. The Investigation of CF_3I For High-Aspect-Ratio Cryogenic Dielectric Etch. In Proceedings of the 2023 China Semiconductor Technology International Conference (CSTIC), Shanghai, China, 26–27 June 2023.
20. Wu, H.; Zhou, Y.; Gao, J.; Peng, Y.; Wang, Z.; Jiang, W. Electrical breakdown in dual-frequency capacitively coupled plasma: A collective simulation. *Plasma Sources Sci. Technol.* **2021**, *30*, 200–221. [CrossRef]
21. Gao, J.; Wu, H.; Yu, S.; Chen, Z.; Wang, Z.; Jiang, W.; Pan, Y. Computational analysis of direct current breakdown process in SF_6 at low pressure. *J. Phys. Appl. Phys.* **2021**, *54*, 32–60. [CrossRef]
22. Georgieva, V. *Computer Modeling of Low-Pressure Fluorocarbon-Based Discharges for Etching Purposes*; Universiteit Antwerpen: Antwerpen, Belgium, 2006; pp. 32–60.
23. Kawaguchi, S.; Satoh, K.; Itoh, H. Electron transport in CF_3I and CF_3I-N_2 mixtures. *Eur. Phys. J.* **2014**, *68*, 1–6. [CrossRef]
24. 2017 Data Group [mbltz Version 10.6]: CF_3I. Available online: https://us.lxcat.net/cache/635b483e31117/ (accessed on 28 September 2022).
25. Christophorou, L.G.; Olthoff, J.K.; Rao, M.J. Electron interactions with CF_3I. *J. Phys. Chem. Ref. Data* **2000**, *29*, 553–569. [CrossRef]
26. Nanbu, K. Probability theory of electron-molecule, ion-molecule, molecule-molecule, and Coulomb collisions for particle modeling of materials processing plasmas and cases. *IEEE Trans. Plasma Sci.* **2000**, *28*, 971–990. [CrossRef]
27. Nanbu, K.; Mitsui, K.; Kondo, S. Self-consistent particle modelling of dc magnetron discharges of an O_2/Ar mixture. *J. Phys. Appl. Phys.* **2000**, *33*, 801–830. [CrossRef]
28. Denpoh, K.; Nanbu, K. Self-consistent particle simulation of radio-frequency CF_4 discharge with implementation of all ion–neutral reactive collisions. *J. Vac. Sci. Technol. A Vac. Surf. Film.* **1998**, *16*, 1201–1206. [CrossRef]

29. De Urquijo, J.; Juárez, A.M.; Basurto, E.; Hernández-Ávila, J.L. Electron impact ionization and attachment, drift velocities and longitudinal diffusion in CF_3I and CF_3I–N_2 mixtures. *J. Phys. Appl. Phys.* **2007**, *40*, 22–30. [CrossRef]

30. Glen, R.C. A fast empirical method for the calculation of molecular polarizability. *J.-Comput.-Aided Mol. Des.* **1994**, *8*, 457–466. [CrossRef]

31. Nanbu, K.; Denpoh, K. Monte Carlo collision simulation of positive-negative ion recombination for a given rate constant. *J. Phys. Soc. Jpn.* **1998**, *67*, 1288–1290. [CrossRef]

32. Verboncoeur, J.P.; Alves, M.V.; Vahedi, V.; Birdsall, C.K. Simultaneous potential and circuit solution for 1D bounded plasma particle simulation codes. *J. Comput. Phys.* **1993**, *104*, 321–328. [CrossRef]

33. Kawamura, E.; Birdsall, C.K.; Vahedi, V. Physical and numerical methods of speeding up particle codes and paralleling as applied to RF discharges. *Plasma Sources Sci. Technol.* **2000**, *9*, 413. [CrossRef]

34. Vahedi, V.; DiPeso, G.; Birdsall, C.K.; Lieberman, M.A.; Rognlien, T.D. Capacitive RF discharges modelled by particle-in-cell Monte Carlo simulation. I. Analysis of numerical techniques. *Plasma Sources Sci. Technol.* **1993**, *2*, 261. [CrossRef]

35. Cohen, B.I.; Langdon, A.B.; Friedman, A. Implicit time integration for plasma simulation. *J. Comput. Phys.* **1982**, *46*, 15–38. [CrossRef]

36. Brackbill, J.U.; Forslund, D.W. An implicit method for electromagnetic plasma simulation in two dimensions. *J. Comput. Phys.* **1982**, *46*, 271–308. [CrossRef]

37. Wang, H.; Jiang, W.; Wang, Y. Implicit and electrostatic particle-in-cell/Monte Carlo model in two-dimensional and axisymmetric geometry: I. Analysis of numerical techniques. *Anal. Numer. Tech.* **2010**, *19*, 15–20. [CrossRef]

38. Wang, H.Y.; Jiang, W.; Sun, P.; Kong, L. On the energy conservation electrostatic particle-in-cell/Monte Carlo simulation: Benchmark and application to the radio frequency discharges. *Chin. Phys.* **2014**, *23*, 35–42. [CrossRef]

39. Jiang, W.; Wang, H.; Bi, Z.; Wang, Y. Implicit and electrostatic particle-in-cell/Monte Carlo model in two-dimensional and axisymmetric geometry: II. Self-bias voltage effects in capacitively coupled plasmas. *Plasma Sources Sci. Technol.* **2011**, *20*, 50–62. [CrossRef]

40. Peng, Y.; Jiang, W.; Innocenti, M.E.; Zhang, Y.; Hu, X.; Zhuang, G.; Lapenta, G. On the breakdown modes and parameter space of ohmic tokamak start-up. *J. Plasma Phys.* **2018**, *84*, 84–95. [CrossRef]

41. Babaeva, N.Y.; Zhang, C.; Qiu, J.; Hou, X.; Tarasenko, V.F.; Shao, T. The role of fast electrons in diffuse discharge formation: Monte Carlo simulation. *Plasma Sources Sci. Technol.* **2017**, *26*, 85–90. [CrossRef]

42. Horváth, B.; Daksha, M.; Korolov, I.; Derzsi, A.; Schulze, J. The role of electron induced secondary electron emission from SiO_2 surfaces in capacitively coupled radio frequency plasmas operated at low pressures. *Plasma Sources Sci. Technol.* **2017**, *26*, 124–130. [CrossRef]

43. Gao, Q.; Niu, C.; Adamiak, K.; Yang, A.; Rong, M.; Wang, X. Numerical simulation of negative point-plane corona discharge mechanism in SF_6 gas. *Plasma Sources Sci. Technol.* **2018**, *27*, 115001. [CrossRef]

44. Takeda, T.; Matsuoka, S.; Kumada, A.; Hidaka, K. Insulation performance of CF_3I and its by-products by sparkover discharge. In Proceedings of the International Conference on Electrical Engineering, Mexico City, Mexico, 5–7 September 2018.

45. Ngoc, M.N.; Denat, A.; Bonifaci, N.; Lesaint, O.; Daoud, W.; Hassanzadeh, M. Electrical breakdown of CF_3I and CF_3I-N_2 gas mixtures. In Proceedings of the 2009 IEEE Conference on Electrical Insulation and Dielectric Phenomena, Virginia Beach, VA, USA, 18–21 October 2009.

46. Xiao, S.; Zhang, X.; Tang, J.; Liu, S. A review on SF_6 substitute gases and research status of CF_3I gases. *Energy Rep.* **2018**, *4*, 486–496. [CrossRef]